Peer review status:

This is a non-peer-reviewed preprint submitted to EarthArXiv.

Enhanced weathering and its potential connection to ocean oxygenation and eukaryotic evolution at 1.57 Ga

Xi Chen[1,2]*, Ying Zhou[1,3], Simon W. Poulton[4], Fred T. Bowyer[5], Colin Mettam[1], Shihong Zhang[6], Maoyan Zhu[7,8], Da Li[9], Philip A.E. Pogge von Strandmann[1,3], Benjamin J. W. Mills[4], Graham A. Shields[1]

[1] LOGIC, Department of Earth Sciences, University College London, London, UK

[2] School of Ocean and Earth Science, University of Southampton, Southampton, UK.

[3] MIGHTY, Institute of Geosciences, Johannes Gutenberg University, Mainz, Germany

[4] School of Earth and Environment, University of Leeds, Leeds LS2 9JT, UK

[5] School of Geosciences, University of Edinburgh, Edinburgh, UK

[6] State key Laboratory of Biogeology and Environmental Geology, China University of Geosciences, Beijing, China

[7] State Key Laboratory of Palaeobiology and Stratigraphy, Nanjing Institute of Geology and Palaeontology, Chinese Academy of Sciences, Nanjing, China

[8] College of Earth and Planetary Sciences, University of Chinese Academy of Sciences, Beijing, China

[9] School of Marine Science and Engineering, Nanjing Normal University, Nanjing, China

*Corresponding author. Email: Xi.Chen@soton.ac.uk

Abstract

Chemical weathering is a critical Earth system process that regulates climate, ocean chemistry and the long-term carbon cycle. During the mid-Proterozoic (~1.8–0.8 Ga), chemical weathering is generally considered to have been relatively muted, but this perception remains largely untested, limiting our understanding of the drivers of purported oxygenation events and coeval biological evolution. Here, we report the first coupled positive seawater $^{87}Sr/^{86}Sr$ (~0.0007) and $\delta^{7}Li$ (~5‰) isotope excursion of the Mesoproterozoic Era (1.6–1.0 Ga). Geochemical box modelling suggests the concurrent Sr - Li isotope excursions signify a substantial weathering event at ~1.57 Ga, characterised by increased silicate weathering rates and decreased weathering congruency. Drawing on independent geological evidence, we posit that enhanced volcanic CO_2 degassing, possibly alongside accretional orogenesis, increased denudation rates and invigorated the hydrological cycle, amplifying silicate weathering and secondary clay formation. This weathering pulse coincided with the ocean oxygenation and carbon cycle disruption, implicating it in the coeval preservation of the earliest known decimetre-scale, multicellular eukaryotic fossils.

1. Introduction

Chemical weathering of silicate minerals sequesters CO_2 and drives marine carbonate precipitation by increasing the supply of dissolved cations and alkalinity to the oceans (Walker et al., 1981; West et al., 2005). Chemical weathering also provides critical nutrients (Fe, P, Si, etc.) to the coastal oceans, thereby promoting primary productivity (Berner, 2003). Therefore, understanding the dynamics of weathering conditions and their controlling factors is crucial to deciphering past changes to global climate, the carbon cycle, redox conditions and biological evolution. The mid-Proterozoic (1.6–1.0 Ga) has been long recognised as a time of unusually muted variability in terms of climate (Holland, 2006), tectonics (Cawood and Hawkesworth, 2014) and ocean-atmosphere composition (Brasier and Lindsay, 1998; Bartley and Kah, 2004; Chen et al., 2022b). Although recent work has highlighted that environmental conditions during the Mesoproterozoic Era were more dynamic than once thought (Zhu et al., 2016; Javaux and Knoll, 2017; Canfield et al., 2018; Gervais et al., 2023), Mesoproterozoic

weathering regimes remain largely unconstrained, hindering our understanding of environmental and biological evolution during Earth's middle age.

One factor that has hampered investigation of Mesoproterozoic weathering is a scarcity of high-quality weathering proxy records (Kalderon-Asael et al., 2021; Chen et al., 2022b), such as Sr ($^{87}Sr/^{86}Sr$) and Li (δ^7Li) isotope ratios. Marine carbonate Sr and Li isotope records can represent robust archives of the Sr and Li isotope composition of ambient seawater, and in combination, have been successfully applied to constrain past weathering behaviour and climate change (Pogge von Strandmann et al., 2013; Caves Rugenstein et al., 2019; Cao et al., 2022). Strontium and Li isotopes are homogeneously distributed in seawater on a global scale, due to their much longer modern ocean residence times (~10^6 years) relative to the time it takes for oceans to circulate (~10^3 years) (Elderfield, 1986; Huh et al., 1998). The Sr isotope budget of seawater is normally used to trace the relative importance of more radiogenic riverine input versus less radiogenic hydrothermal input (Spooner, 1976), but its interpretation is complicated by the large isotopic range of lithologies undergoing weathering (Halverson et al., 2010; Bataille et al., 2017; Peucker-Ehrenbrink and Fiske, 2019). Strontium isotopes in seawater are incorporated into carbonate minerals through substitution for calcium, without isotopic fractionation (McArthur, 1994).

By contrast, riverine δ^7Li values are largely independent of the silicate lithology being weathered, and not affected by weathering of carbonates, but the formation of silicate secondary minerals preferentially consumes ^6Li, driving residual waters to heavier isotopic values. Thus, riverine δ^7Li provides direct information on silicate weathering congruency, reflecting the extent of primary rock dissolution relative to secondary mineral formation (Misra and Froelich, 2012; Pogge von Strandmann and Henderson, 2015), and may also be a tracer for weathering intensity, reflecting the ratio of weathering rate (W) to the denudation rate (D) (Dellinger et al., 2015). The ocean Li reservoir is mainly sourced from riverine and hydrothermal inputs, while the oceanic sinks of Li primarily consist of uptake by low-temperature clays formed during the alteration of oceanic crust (AOC) and the formation of marine aluminous authigenic clays (MAAC) (Chan et al., 1992; Misra and Froelich, 2012). The incorporation of oceanic Li into authigenic clay minerals, a process known as reverse weathering, imparts a combined

fractionation effect of ~14–16‰, which drives modern seawater to ~31‰ (Misra and Froelich, 2012). Seawater lithium isotope compositions (δ^7Li_{sw}) can therefore be used to examine silicate weathering regimes and marine reverse weathering, thus complementing the $^{87}Sr/^{86}Sr_{sw}$ record.

The marine carbonate succession of the ~1.57 Ga Gaoyuzhuang Formation on the North China Craton contains a negative carbon isotope excursion (CIE), with multiple geochemical proxies suggesting a contemporaneous marine oxygenation event (Zhang et al., 2018; Shang et al., 2019; Luo et al., 2020; Tang et al., 2022; Xie et al., 2023; Xu et al., 2023) linked to the appearance of decimetre-scale, multicellular eukaryotic macrofossils (Zhu et al., 2016). Here, we report $^{87}Sr/^{86}Sr$ and δ^7Li isotope ratios for marine carbonate rocks of the Gaoyuzhuang Formation, to reconstruct the weathering regime across this oxygenation event. We then utilise a geochemical box model to explore the driving mechanisms behind the weathering regime shift we document. Combined with published redox proxies, we subsequently consider plausible links between tectonics, climate, weathering, redox and biological evolution during the early Mesoproterozoic Era.

2. Geological setting

The Gaoyuzhuang Formation is dominated by marine carbonates that were deposited from the deep subtidal to supratidal zones in the Yanliao Basin of the North China Craton (**Fig. 1a**) (Mei, 2006). The Gaoyuzhuang Formation corresponds to a period during the final assembly of the supercontinent Nuna, marked by accretion on its periphery, while extensional processes may have influenced its interior (Zhang et al., 2012a; Pourteau et al., 2018). In ascending order, the Gaoyuzhuang Formation can be divided into four members Member I (Guandi Member), Member II (Sangshu'an Member), Member III (Zhangjiayu Member) and Member IV (Huanxiusi Member). This study focuses on Gaoyuzhuang Member III, which consists mainly of limestone and dolomitic limestone deposited during a transgression-regression cycle (**Fig. 1c**) (Mei, 2006). The nodular limestone, thinly bedded argillaceous (dolomitic) limestone and calcareous mudstone in the lower to middle parts of Member III reflect a deeper water environment, possibly below the storm wave base (Mei, 2006; Guo et al., 2013). The 'molar tooth' limestone and microbial dolostone with ripple marks in the upper part of Member III suggest a shallower,

possibly upper subtidal to intertidal environment (Mei, 2006). Our samples were collected from the Gaoyuzhuang Formation Member III (Zhangjiayu Member) at four different sections (Gangou, Jixian, Kuancheng, Pingquan, **Fig. 1b**). In the lower and upper horizons of Member III, two tuff beds yield U-Pb zircon ages of 1577 ± 12 Ma (Jixian Section; Tian et al., 2015) and 1560 ± 5 Ma (Gangou Section; Li et al., 2010) respectively.

3. Materials and Methods

3.1. Sample preparation method

A total of 223 marine carbonate rocks were selected for this study. Samples were micro-drilled and then ground by hand using an agate pestle and mortar. For bulk carbonate dissolution, ~10–20 mg of sample powder (N = 223) was dissolved in 5 ml of 2% *v/v* HNO_3 for 24 h, then centrifuged at 3600 rpm for 5 mins. The supernatant was collected and diluted with 2% *v/v* HNO_3 for major and trace elemental analysis (e.g., Ca, Mg, Sr, Al, Mn).

For Sr isotope preparation, we followed the newly developed sequential leaching method for argillaceous and dolomitic limestones (Chen and Zhou, 2023), where ~50–100 mg of micro-drilled sample powder (N = 133) was precleaned with 3–5 ml of 1 M ammonium acetate in an ultrasonic bath for 30 mins at room temperature. After centrifugation, the residue was washed once with ultrapure water and centrifuged again. 0.05–0.2 M of acetic acid (HAc), calculated to dissolve ~10–30% carbonate, was then added to the residue. After the acid was added, samples were ultrasonically agitated for 30 mins and then allowed to stand for another 30 mins at room temperature, before being centrifuged at 3600 rpm for 5 mins. The supernatant was collected for Sr isotope and elemental analysis.

For Li isotope preparation, we followed the leaching method of (Tessier et al., 1979), as tested by many recent studies (Pogge von Strandmann et al., 2019, 2021b; Liu et al., 2022a; Krause et al., 2023), where acetic acid was buffered to *p*H 5 with sodium acetate (NaOAc). 0.75 ml of *p*H-buffered solution was added to ~100 mg of micro-drilled sample powder (N = 49), then ultrasonically agitated for 10 mins and left to stand for ~5 h at room

temperature. The solution was then centrifuged, and the supernatant carefully pipetted out for Li isotope and elemental analysis.

3.2. Analytical methods

All geochemical analyses were carried out at the London Geochemistry and Isotope Centre (LOGIC), University College London (UCL). Elemental analyses were performed on solutions of bulk carbonate (2% *v/v* HNO_3) and all supernatant leaches prepared for Sr (in HAc) and Li (in NaOAc) isotopes. Major element concentrations in carbonate leachates, including Ca, Mg, Mn, Al and Sr, were measured by inductively coupled plasma optical emission spectrometry (Varian 720 ICP–OES). Each data point represents the average of 6 replicates, with the RSD being < 3% for all analysed elements. Trace element Rb and Li concentrations of carbonate leachates were analysed by inductively coupled plasma mass spectrometry (Agilent 7900 ICP–MS) with calibration standards (Superco, Sigma–Aldrich) and samples matrix-matched to 50 μg/g Ca (and also to Na content in the case of NaOAc leaches). Each data point represents the average of 7 replicates, with the RSD being < 5% for all the analysed elements.

For Sr isotope analysis, small polypropylene columns with polypropylene frits (~30 μm) and ~1 cm thickness (30–40 mg) of Eichrom® Sr specific resin were used for Sr separation in an ISO 7 (Class 10000) metal-free laboratory with ISO 5 laminar flow hoods at UCL. The supernatant (in 0.05–0.2 M acetic acid) was dried on a hotplate before being dissolved in 0.5 ml of 4 M nitric acid and then passed through the precleaned and conditioned columns. The column was sequentially eluted with 1 ml of 8 M HNO_3, and twice with a full reservoir of 8 M HNO_3 to primarily wash out the matrix. Afterwards, two full reservoirs of Milli-Q water were used to elute Sr. The collected eluant was then dried and redissolved in 2% *v/v* HNO_3 for conventional $^{87}Sr/^{86}Sr$ isotope analysis. The $^{87}Sr/^{86}Sr$ isotope ratios were measured using a Nu Instruments Plasma 3 multi-collector inductively coupled plasma mass spectrometer (MC–ICP–MS) at UCL. Instrumental isotopic fractionation (IIF) was corrected using the exponential law (to $^{86}Sr/^{88}Sr = 0.1194$), followed by a standard bracketing method. The interferences of ^{87}Rb were corrected using an $^{87}Rb/^{85}Rb$ ratio of 0.3857. Interferences for Kr were corrected by a

blank measurement before each sample. Reported $^{87}Sr/^{86}Sr$ ratios were corrected to the published value of SRM 987 (0.710252 ± 0.000013; Weis et al., 2006). An in-house carbonate standard (N1, modern shell) was processed along with sample leachates and its multi-run average was 0.70918 ± 0.000018 (2 SD, N=10), which is comparable to the modern seawater value (0.709175 ± 0.0000012; Kuznetsov et al., 2012). A procedural blank was included in each batch of samples, with Sr quantities of less than 0.01% contribution to sample measurements.

For Li isotope analysis, a two cation-exchange column method was used for Li purification at the LOGIC laboratories (Pogge von Strandmann et al., 2019; Liu et al., 2022a). AG®50 W X-12 resin was used for the cation-exchange procedure and eluted by 0.2 M HCl. Li isotope fractionation during column elution was also monitored by collecting a split of the elution before and after the Li collection, which was then analysed for Li content. All splits had < 0.2% of the total Li, which means the shift in Li isotopes caused by incomplete recovery from columns was less than the long-term precision of the Li isotope ratio measurements (Pogge von Strandmann et al., 2021a; Liu et al., 2022a). Lithium isotopes were measured by a multi-collector ICP-MS (Nu Plasma 3) at UCL. A sample-standard (IRMM-016) bracketing method was applied for Li isotope measurement. A procedural blank was included in each batch of samples with Li quantities of less than 0.03% contribution to the sample measurements. Each sample was measured a total of three times with ten ratios (50 s total integration time) for each time. The Li isotope data are reported as the deviation of the $^{7}Li/^{6}Li$ ratio in samples from the zero-reference material L-SVEC ($^{7}Li/^{6}Li$ = 12.17285 ± 0.00023; Magna et al., 2004), which has same isotope ratio as IRMM-016 (Jeffcoate et al., 2004). The reproducibility and accuracy of the Li procedure, including sample digestion, Li separation and Li isotope analysis were checked by repeated measurements of Atlantic seawater ($\delta^{7}Li$ = 31.08‰ ± 0.48‰ relative to L-SVEC, 2 SD, N = 6). Further standards analysed by this method are reported in Pogge von Strandmann et al. (2019).

For C and O isotope analysis, powdered carbonate (N = 192) was analysed at the Bloomsbury Environmental Isotope Facility (BEIF) at UCL on a continuous-flow (ThermoFisher Delta V) mass spectrometer linked to a Gas

Bench II device. All values are reported using the Vienna Pee Dee Belemnite notation (VPDB) relative to NBS19. Repeat measurements of the standard NBS 19 gave $\delta^{13}C_{VPDB}$ = 1.95‰ ± 0.06‰ (2 SD, N = 12), $\delta^{18}O_{VPDB}$ = −2.2‰ ± 0.1‰ (2 SD, N = 12).

4. Results and discussion

4.1. Seawater strontium and lithium isotope records

Strontium, Li, C ($\delta^{13}C_{carb}$) and O ($\delta^{18}O_{carb}$) isotopes, as well as major and trace elements are reported in this study (**Supplementary Data S1**) for marine carbonate rocks across four sections of the GYZ Formation Member III**.** The characteristic negative C isotope excursion of Member III is observed in three sections (Pingquan, Jixian and Gangou; note that its absence in the Kuancheng section reflects lack of exposure), with a robust $\delta^{13}C_{carb}$ shift from ~0‰ to ~-4‰ (**Fig. 1d, e**), with no signs of diagenetic overprinting (see **Supplementary Information**; **Fig. S1**). A floating astronomical timescale has been established based on Milankovitch cycles extracted from Member III of the Gaoyuzhuang Formation in the Jixian and Gangou sections (Liu et al., 2022b). Age models and stratigraphic correlations are constructed based on carbon isotope stratigraphy, cyclostratigraphy, and the published dating constraints (**Fig. 1d,e** and see **Supplementary Information for details).**

Following petrographic observation and a four-step geochemical screening approach (diagenesis evaluation, clay contamination evaluation, cut-off validity evaluation, section comparison; see **Supplementary Information, Figs. S2-S6**), we selected samples with no discernible geochemical evidence for significant alteration to reconstruct the Sr and Li isotopic evolution of contemporaneous seawater. Seawater $\delta^{7}Li$ values were estimated from measured rock values by the addition of 5‰ on average (full range 3–8.5‰) (Marriott et al., 2004; Pogge von Strandmann et al., 2013; Pogge von Strandmann et al., 2019; Day et al., 2021; Krause et al., 2023), to correct for isotopic fractionation during Li incorporation into carbonates (see **Supplementary Information**). The seawater $^{87}Sr/^{86}Sr$ and $\delta^{7}Li$ values for the three sections that document the C isotope excursion show a coupled increasing trend towards the nadir of the $\delta^{13}C_{carb}$ excursion (-4‰), with a Sr isotope increase from ~0.7050 to

~0.7057 and a Li isotope increase from ~13‰ to ~18‰ (**Fig. 2**). After reaching peak values, Sr isotope ratios decrease to ~0.7048, before returning to ~0.7050, while Li isotope values return to ~13‰ and remain around this level. $\delta^{13}C_{carb}$ values likewise recover to a consistent value of ~0‰. The screened samples from different sections exhibit the same secular trend for both Sr and Li isotopes, supporting the robustness of our approach to screening and correlation **(Fig. 2).**

4.2. Modelling the Sr and Li positive isotope excursion

Dynamic Sr and Li isotope box models have been developed by previous studies (Pogge von Strandmann et al., 2013; Nana Yobo et al., 2021; Pogge von Strandmann et al., 2021b), and are used here to constrain which of the key potential factors (including the hydrothermal flux, river input flux and its isotope composition, and marine reverse weathering) are the likely controls on the observed covariation in Li and Sr isotopes. Our model for seawater Sr and Li isotopes is solved in 10 kyr steps, and the model structure and input parameters are detailed in the **Supplementary Information** and **Table S1**. The modern oceanic residence times for Sr and Li isotopes are initially set in alignment with previous modelling studies conducted for the Precambrian (Kalderon-Asael et al., 2021).

Based on the current age model, δ^7Li (from ~13‰ to ~18‰) and $^{87}Sr/^{86}Sr$ (from ~0.705 to 0.7057) increased to peak values within ~1 Myr (**Fig. 2**). Using our box model, if a decreased hydrothermal flux was the only driving factor, then a ≥10 times decrease in hydrothermal flux is required to achieve the Sr isotope peak. However, even such a substantial decrease in hydrothermal flux would only result in an ~2‰ increase in Li isotope values (**Fig. S7a**). Increasing the weathering flux without altering the isotopic values would lead to an increase in seawater $^{87}Sr/^{86}Sr$, as river input is more radiogenic than seawater in our model (**Supplementary Information**). However, since the riverine input δ^7Li is lower than that of seawater (due to marine clay minerals preferentially incorporating ^{6}Li), this increased weathering flux would lead to a decrease, rather than an increase, in seawater δ^7Li (**Fig. S7b**).

Conversely, if a consistent weathering flux was accompanied by simultaneous increases in riverine Li and Sr isotope values, then an increase within 1 Myr of ~14.5‰ and ~0.0035, respectively, would be required to attain the peak values (**Fig. S7c**). Such a substantial increase (~0.0035) in the riverine Sr isotope ratio, however, appears improbable, as it surpasses both the magnitude of the shift in riverine $^{87}Sr/^{86}Sr$ ratios resulting from Himalayan erosion and weathering over the last 40 Myr (Richter et al., 1992), and the net impact of the highly radiogenic Ganges-Brahmaputra system on the contemporary oceanic Sr budget (Richter and Turekian, 1993). Therefore, changes to both the riverine flux and its isotopic composition would appear necessary to explain our data. We thus use the seawater $^{87}Sr/^{86}Sr$ ratio to constrain the weathering flux change (assuming an unchanging riverine input Sr isotope value; see **Supplementary Information**), which is subsequently applied to the Li isotope system to constrain variability in riverine δ^7Li. This approach replicates the positive excursion with a 2.8 times increase in the continental weathering flux (Fr), coupled with an ~12‰ (full range 10–13‰) increase in riverine δ^7Li (**Fig. 3a, 3b**).

Another possibility to explain seawater Li isotope variability concerns an increase in the fractionation factor ($\Delta Li_{sw\text{-}sink}$) during marine reverse weathering. Extensive and rapid marine reverse weathering has been proposed for the Precambrian (Krissansen-Totton and Catling; Isson and Planavsky, 2018; Kalderon-Asael et al., 2021), attributable mainly to silica oversaturation, with a possible influence from elevated marine concentrations of other clay-forming elements (such as Fe) in the ferruginous (anoxic and Fe-rich) ocean interior (Poulton and Canfield, 2011). Enhanced reverse weathering could have led to a reduced Li isotopic fractionation between seawater and marine clay minerals (Kalderon-Asael et al., 2021). Given the increased riverine flux (2.8 times) constraint from Sr isotopes, an increase in $\Delta Li_{sw\text{-}sink}$ to 21‰ would be required to explain the coeval Li isotope excursion (**Fig. S7d**). This value is even higher than the modern value (~16‰) (Misra and Froelich, 2012), which seems unlikely, as the biologically controlled Si cycle that dominates today was absent in the Precambrian, and there was no known evidence for widespread chert deposition during the study interval (Krissansen-Totton and Catling). Other effects, such as temperature and pH changes, are also unlikely to have driven the observed Li isotope shifts (see **Supplementary Information**). Therefore, the scenario of increased continental weathering coupled with

increased river δ^7Li remains the most plausible explanation for the coupled positive Sr-Li isotope excursion at ~1.57 Ga. Different combinations of input parameters such as simultaneous changes in Sr isotope composition and fluxes might yield similar model outcomes. While the absolute values may vary, an increase in weathering flux, accompanied by elevated riverine δ^7Li, remains a necessary feature that reproduce the observed increasing trend (**Supplementary Information**).

After reaching peak values, δ^7Li returned to its initial value, while $^{87}Sr/^{86}Sr$ declined to a lower than initial value (0.70484), within ~1.2 Myr. The observed recovery trend cannot be fully explained by scenarios such as solely decreasing riverine input values or altering the weathering flux (**Supplementary Information and Fig. S8**). Given modern oceanic residence times, a twofold increase in hydrothermal input is necessary to account for the decreasing trend in $^{87}Sr/^{86}Sr$ ratios. However, this change alone cannot restore seawater δ^7Li to its initial value, as marine $^{87}Sr/^{86}Sr$ is considerably more sensitive to hydrothermal input than δ^7Li (Pogge von Strandmann et al., 2013). An additional decrease in riverine δ^7Li to zero or a negative value would be required to match the observed trend (**Fig. 3b**, solid line). Such a decrease, however, is less realistic as it would imply riverine δ^7Li values lower than the average for primary silicate rocks (Pogge von Strandmann et al., 2021a).

Alternatively, a reduction in the oceanic residence times of Sr and Li would lead to a more rapid recovery. If we assume that Li removal to marine authigenic clays was more prevalent during the Precambrian (Kalderon-Asael et al., 2021), resulting in minimal isotopic fractionation, this would imply a lower seawater Li inventory. Consequently, a reduced residence time for Li isotopes is highly likely. However, this assumption does not apply to strontium isotopes, and an external forcing is necessary to achieve lower $^{87}Sr/^{86}Sr$ ratios during the recovery phase, relative to the initial values. Given the weathering and hydrothermal flux constrained by Sr isotopes with a modern residence time, a reduced residence time for Li isotopes allows its recovery without further decreasing of riverine δ^7Li values (**Fig. 3b, dash line**). Within the framework of partial breakup of the supercontinent Nuna (Lu et al., 2002), and excluding other potential scenarios, the recovery of Sr and Li isotope ratios might reasonably be attributed to an increased hydrothermal input, with the reduced residence time for the Li reservoir (**Fig. 3a, 3b**). Details of failed recovery scenarios are provided in the **Supplementary Information**.

The scenario presented here represents the most plausible interpretation based on the current age model. The excursion duration (~2 Myr) used in this study is derived from the age model constructed using central ages of two U–Pb zircon dates (1560 Ma to 1577 Ma). Independent constraints from the Sr isotope record suggest that a minimum of ~4 Myr may be required to account for the observed increase of ~0.0007 in our data (see **Supplementary Information**). This makes a significantly shorter duration than 2 Myr unlikely. Therefore, our use of a ~2 Myr excursion duration likely represents a minimum-case scenario, and the associated weathering/hydrothermal flux estimates could be regarded as maximum constraints. Sensitivity tests relating to uncertainties of the age model, varying excursion durations and initial input parameters (e.g., hydrothermal input flux and $\Delta Li_{sw\text{-}sink}$ fractionation factors) are discussed in the **Supplementary Information** (**Figs. S9-S12**).

4.3. Changes in weathering regime and its possible driving mechanisms

In modern settings, riverine (dissolved) δ^7Li plotted against weathering intensity shows a "boomerang" shape, whereby the highest riverine δ^7Li corresponds to a moderate weathering intensity with increased clay formation (incongruent weathering; Dellinger et al., 2015; Pogge von Strandmann et al., 2021b), while the dissolved Li yield (weathering flux) decreases towards the high-intensity regime (Pogge von Strandmann et al., 2021b). Our modelling results indicate that the increasing trend observed for the Sr-Li isotope excursion is primarily driven by an enhanced continental weathering flux, coupled with elevated riverine δ^7Li. This model result aligns with a weathering regime shift from high intensity (transport-limited and congruent weathering) towards moderate intensity (higher denudation rates and incongruent weathering).

A decrease in weathering intensity with an increased weathering flux may have been driven either by warming episodes (increase in CO_2 degassing; Pogge von Strandmann et al., 2013; Krause et al., 2023) or by increased tectonic uplift with more fresh rocks being exposed and weathered (Misra and Froelich, 2012; Caves Rugenstein et al., 2019). Although tectonic uplift seems unlikely to fit an event of such short duration, the influence of orogenic activity cannot be fully dismissed. The final stages of Nuna assembly likely occurred ~1.6 Ga (Pourteau et al., 2018) through the collision between north Australia and Laurentia, and palaeocontinental reconstruction

suggests that the North China Craton was then connected to the North Australia Craton (Zhang et al., 2012a). The estimated high pCO_2 levels across the study interval (Zhang et al., 2022) suggest the presence of an external carbon source to offset carbon consumption by higher weathering rates. CO_2 degassing from intensive volcanism during this period is supported by Hg enrichment in marine sediments (Tang et al., 2022), the presence of large igneous provinces (Baratoux et al., 2019; Teixeira et al., 2019), and a potentially global plume event (Condie et al., 2023) across and preceding the excursion (**Fig. 2**). Increased pCO_2 would have enhanced global surface temperatures, leading to an intensified hydrological cycle and increased rainfall (Krause et al., 2023). In the meantime, the orogenic activity and volcanic eruptions may have supplied more weatherable fresh rock surfaces. As a result, the denudation rate (D) would have increased (Pogge von Strandmann et al., 2021b), leading to enhanced clay mineral formation, resulting in increased incongruent weathering and elevated riverine δ^7Li values. An analogous silicate weathering scenario has been observed in the Cenozoic Era (Krause et al., 2023), when increased clay formation sequestered carbonate-forming cations, thus playing a key role in sustaining the Middle Eocene Climatic Optimum. This scenario also aligns well with the sustained high pCO_2 levels and warm climate during the study period. The integration of our data, geological evidence and modelling outcomes therefore supports the hypothesis of a volcanism-induced weathering event affecting tectonically uplifted terrains, triggering an increase in continental weathering rates and a decrease in weathering congruency.

4.4. Links to the Mesoproterozoic carbon cycle and ocean oxygenation

Seawater $^{87}Sr/^{86}Sr$ and δ^7Li values initially increased prior to the negative CIE, but their peak and falling limb coincide with the nadir and recovery of $\delta^{13}C_{carb,}$ respectively (**Fig. 2**). An increase in the isotopic composition of carbonate-associated sulfate ($\delta^{34}S_{CAS}$) occurs almost coincident with increasing seawater Sr and Li isotopes, followed by a sharp decline below the CIE (Xie et al., 2023), while positive I/(Ca+Mg) and P/Al excursions occur prior to and across the CIE (**Fig. 2**). Multiple studies based on independent redox proxies (e.g., $\delta^{53}Cr$, $\delta^{98}Mo$, I/(Ca+Mg) ratios, $\delta^{34}S_{CAS}$, Ce anomalies) have suggested that the negative carbon isotope excursion in GYZ Member III most likely resulted from an oceanic oxygenation event (Zhang et al., 2018; Shang et al., 2019; Luo et

al., 2020; Tang et al., 2022; Xie et al., 2023; Xu et al., 2023). Based on these observations, we propose a plausible connection between the changes in the weathering regime and the associated carbon cycle perturbations, ocean oxygenation, and biological evolution that occurred during deposition of the GYZ Formation.

Initially, the weathering regime was transport-limited, characterised by low δ^7Li and $^{87}Sr/^{86}Sr$ ratios (as discussed above), with low riverine sulfate and nutrient inputs (Guo et al., 2015; Xie et al., 2023) (**Fig. 4a**). Intensified volcanic CO_2 degassing alongside tectonic uplift triggered greater continental weathering and a possible increase in the sulfate influx to the oceans (Shields et al., 2019). Given the low seawater sulfate concentrations envisaged for this interval (Guo et al., 2015; Xie et al., 2023), an initial increase in nutrient inputs through weathering led to sulfate-limited pyrite burial, potentially combined with greater isotopic fractionation during microbial sulfate reduction (Habicht et al., 2002), resulting in a positive shift in measured $\delta^{34}S_{CAS}$ (Xie et al., 2023). Continued weathering, indicated by Sr and Li isotope peaks, may then have triggered a pulse of sulfate into the ocean, thus overturning the effects of pyrite burial on seawater $\delta^{34}S$ due to a combination of a lower proportion of pyrite burial relative to the sulfate input, and a greater flux of isotopically lighter riverine sulfate (Shields et al., 2019) (**Fig. 4b**). Enhanced continental weathering would also have delivered the essential nutrient P to the ocean, promoting marine productivity and organic carbon burial (**Fig. 4b**).

A combination of enhanced organic carbon and pyrite burial potentially raised atmospheric oxygen levels, as supported by recent findings of positive chromium isotope values immediately prior to the carbon isotope excursion (Tang et al., 2022; Xie et al., 2023). Molybdenum isotope modelling suggests that atmospheric O_2 levels could have temporarily reached ~4% PAL, possibly even up to ~30% PAL (Xu et al., 2023), contributing to widespread marine oxygenation, as indicated by a marked increase in carbonate-bound I/(Ca+Mg) (Shang et al., 2019). Although an increased organic carbon burial is typically associated with a positive CIE, the Proterozoic carbon isotope record has been proposed to be insensitive to such changes due to counterbalancing effects from the weathering of isotopically light organic carbon (Daines et al., 2017). Increased sulfate weathering, linked to pyrite burial, may have served as a potential oxygen source (Shields et al., 2019), as evidenced by the positive $\delta^{34}S_{CAS}$ isotope excursion (**Fig. 2**).

The increased availability of oxidants in the ocean, such as sulfate and oxygen, likely led to remineralization (oxidation) of the marine dissolved organic matter pool (DOM; Rothman et al., 2003), releasing organic-bound carbon, and eventually causing the $\delta^{13}C_{carb}$ composition of marine dissolved inorganic carbon to decrease (Chen et al., 2022a; Shi et al., 2022). The release of organically bound P and C through the oxidation of DOM would have resulted in elevated oceanic P and atmospheric CO_2 levels (Alcott et al., 2022; Dodd et al., 2023). The increased pCO_2 would then have sustained or further accelerated silicate weathering and P input to the ocean, which may explain the peaks in P and Sr-Li isotopes observed across the negative CIE (**Fig. 4b**). As the available oxidant (e.g., O_2, SO_4) in the ocean was limited by the presence of a DOM reservoir and a relatively small sulfate reservoir, ocean oxidation would not have been sustained, leading to a return to initial $\delta^{13}C_{carb}$ values (**Fig. 4c**). Cessation of DOM oxidation and reduced continental weathering would then have reduced the P input to the ocean, thus decreasing organic carbon and pyrite burial, leading to a return to more widespread anoxia (**Fig. 4c**).

Similar to the redox status of the Ediacaran ocean, which was characterized by dramatic redox oscillations with multiple transient oxygenation events (Sahoo et al., 2012; Chen et al., 2022a), the Mesoproterozoic has also emerged as a rather dynamic interval that experienced significant variability in the extent of carbon perturbation and ocean oxygenation (Chu et al., 2007; Diamond et al., 2021). While the influence of oxygen on biological evolution remains a topic of debate, some studies (Shang et al., 2019; Xu et al., 2023) have proposed that oxygen levels in the early Mesoproterozoic ocean may have (at least intermittently) surpassed the threshold required for the last common ancestor of animals (0.5–4% PAL; Mills et al., 2014), potentially creating conditions favourable to the evolution of multi-cellularization in early eukaryotes at this time. Although similar eukaryote-grade fossil organisms are found both below and above this level, the GYZ fossils are remarkable for their unprecedented size (reaching up to 30 cm in length and nearly 8 cm in width) with fossils of comparable scale not reappearing for nearly a billion years (Zhu et al., 2016). This temporal coincidence highlights a plausible link between the transient oxygenation event, likely driven by enhanced weathering, and the increase in eukaryotic body size.

More broadly, enhanced weathering and increased productivity in a greenhouse world shaped by volcanic activity (LIPs) can trigger oceanic anoxia and mass extinctions during predominantly oxic oceanic conditions, as is

evident during the Phanerozoic (Turgeon and Creaser, 2008). However, during the Mesoproterozoic, when oceans were low in oxygen, such volcanic activity may have contributed to oxygen accumulation in surface oceans, thereby promoting biological innovation. Our study suggests that the impacts of volcanic activity may vary significantly depending on environmental conditions, thereby yielding new insight into controls on the coevolution of life and the environment through Earth's middle age.

5. Conclusion

Our study presents the first evidence of a coupled positive Sr and Li isotope excursion in the early Mesoproterozoic seawater, revealing a significant weathering event at approximately 1.57 Ga. This event was characterised by an increased chemical weathering rate alongside decreased weathering congruency. We propose that the onset of this weathering pulse was primarily driven by elevated CO_2 emissions from intense volcanic activity, possibly accompanied by orogenic processes. Enhanced weathering increased the delivery of nutrients and sulfate to the ocean, stimulating the burial of organic carbon and pyrite. This process elevated the concentrations of marine oxidants, such as sulfate and oxygen, which may have facilitated the oxidation of the dissolved organic carbon pool and contributed to the concurrent negative carbon isotope excursion. The resulting oxygenation event may have created more favourable conditions for the emergence and preservation of decimetre-scale, multicellular eukaryotic organisms in the early Mesoproterozoic Era.

References

Alcott, L.J., Mills, B.J.W., Bekker, A., and Poulton, S.W., 2022, Earth's Great Oxidation Event facilitated by the rise of sedimentary phosphorus recycling: Nature Geoscience, v. 15, doi:10.1038/s41561-022-00906-5.

Baratoux, L. et al., 2019, New U–Pb baddeleyite ages of mafic dyke swarms of the west African and amazonian cratons: Implication for their configuration in supercontinents through time, *in* Springer Geology, doi:10.1007/978-981-13-1666-1_7.

Bartley, J.K., and Kah, L.C., 2004, Marine carbon reservoir, Corg-Ccarb coupling, and the evolution of the Proterozoic carbon cycle: Geology, v. 32, doi:10.1130/G19939.1.

Bataille, C.P., Willis, A., Yang, X., and Liu, X., 2017, Continental igneous rock composition: A major control of past global chemical weathering: Science Advances, v. 3, p. 1–16, doi:e1602183.

Berner, R.A., 2003, The long-term carbon cycle, fossil fuels and atmospheric composition: Nature, v. 426, doi:10.1038/nature02131.

Brasier, M.D., and Lindsay, J.F., 1998, A billion years of environmental stability and the emergence of eukaryotes: new data from northern Australia: Geology, v. 26, doi:10.1130/0091-7613(1998)026<0555:ABYOES>2.3.CO;2.

Canfield, D.E., Zhang, S., Frank, A.B., Wang, X., Wang, H., Su, J., Ye, Y., and Frei, R., 2018, Highly fractionated chromium isotopes in Mesoproterozoic-aged shales and atmospheric oxygen: Nature Communications, v. 9, doi:10.1038/s41467-018-05263-9.

Cao, C., Bataille, C.P., Song, H., Saltzman, M.R., Tierney Cramer, K., Wu, H., Korte, C., Zhang, Z., and Liu, X.M., 2022, Persistent late Permian to early Triassic warmth linked to enhanced reverse weathering: Nature Geoscience, v. 15, doi:10.1038/s41561-022-01009-x.

Caves Rugenstein, J.K., Ibarra, D.E., and von Blanckenburg, F., 2019, Neogene cooling driven by land surface reactivity rather than increased weathering fluxes: Nature, v. 571, p. 99–102, doi:10.1038/s41586-019-1332-y.

Cawood, P.A., and Hawkesworth, C.J., 2014, Earth's middle age: Geology, v. 42, p. 503–506, doi:10.1130/G35402.1.

Chan, L.H., Edmond, J.M., Thompson, G., and Gillis, K., 1992, Lithium isotopic composition of submarine basalts: implications for the lithium cycle in the oceans: Earth and Planetary Science Letters, v. 108, doi:10.1016/0012-821X(92)90067-6.

Chen, B. et al., 2022a, A short-lived oxidation event during the early Ediacaran and delayed oxygenation of the Proterozoic ocean: Earth and Planetary Science Letters, v. 577, doi:10.1016/j.epsl.2021.117274.

Chen, X., and Zhou, Y., 2023, Effective leaching of argillaceous and dolomitic carbonate rocks for strontium isotope stratigraphy: Geostandards and Geoanalytical Research, v. 48, doi:10.1111/ggr.12531.

Chen, X., Zhou, Y., and Shields, G.A., 2022b, Progress towards an improved Precambrian seawater 87Sr/86Sr curve: Earth-Science Reviews, v. 224, doi:10.1016/j.earscirev.2021.103869.

Chu, X., Zhang, T., Zhang, Q., and Lyons, T.W., 2007, Sulfur and carbon isotope records from 1700 to 800 Ma carbonates of the Jixian section, northern China: Implications for secular isotope variations in Proterozoic seawater and relationships to global supercontinental events: Geochimica et Cosmochimica Acta, v. 71, doi:10.1016/j.gca.2007.07.017.

Condie, K.C., Pisarevsky, S.A., Puetz, S.J., Roberts, N.M.W., and Spencer, C.J., 2023, A-type granites in space and time: Relationship to the supercontinent cycle and mantle events: Earth and Planetary Science Letters, v. 610, doi:10.1016/j.epsl.2023.118125.

Daines, S.J., Mills, B.J.W., and Lenton, T.M., 2017, Atmospheric oxygen regulation at low Proterozoic levels by incomplete oxidative weathering of sedimentary organic carbon: Nature Communications, v. 8, doi:10.1038/ncomms14379.

Day, C.C., Pogge von Strandmann, P.A.E., and Mason, A.J., 2021, Lithium isotopes and partition coefficients in inorganic carbonates: Proxy calibration for weathering reconstruction: Geochimica et Cosmochimica Acta, v. 305, doi:10.1016/j.gca.2021.02.037.

Dellinger, M., Gaillardet, J., Bouchez, J., Calmels, D., Louvat, P., Dosseto, A., Gorge, C., Alanoca, L., and Maurice, L., 2015, Riverine Li isotope fractionation in the Amazon River basin controlled by the weathering regimes: Geochimica et Cosmochimica Acta, v. 164, p. 71–93, doi:10.1016/j.gca.2015.04.042.

Diamond, C.W., Ernst, R.E., Zhang, S.H., and Lyons, T.W., 2021, Breaking the Boring Billion: A Case for Solid-Earth Processes as Drivers of System-Scale Environmental Variability During the Mid-Proterozoic, *in* Large Igneous Provinces: A Driver of Global Environmental and Biotic Changes, doi:10.1002/9781119507444.ch21.

Dodd, M.S. et al., 2023, Uncovering the Ediacaran phosphorus cycle: Nature, v. 618, doi:10.1038/s41586-023-06077-6.

Elderfield, H., 1986, Strontium isotope stratigraphy: Palaeogeography, Palaeoclimatology, Palaeoecology, v. 57, doi:10.1016/0031-0182(86)90007-6.

Gervais, F., Beaudry, A., Kavanagh-Lepage, C., Moukhsil, A., Larson, K.P., and Guilmette, C., 2023, Far from boring: A new Grenvillian perspective on Mesoproterozoic tectonics: Earth and Planetary Science Letters, v. 610, doi:10.1016/j.epsl.2023.118129.

Guo, H., Du, Y., Kah, L.C., Hu, C., Huang, J., Huang, H., Yu, W., and Song, H., 2015, Sulfur isotope composition of carbonate-associated sulfate from the Mesoproterozoic Jixian Group, North China: Implications for the marine sulfur cycle: Precambrian Research, v. 266, doi:10.1016/j.precamres.2015.05.032.

Guo, H., Du, Y., Kah, L.C., Huang, J., Hu, C., Huang, H., and Yu, W., 2013, Isotopic composition of organic and inorganic carbon from the Mesoproterozoic Jixian Group, North China: Implications for biological and oceanic evolution: Precambrian Research, v. 266, doi:10.1016/j.precamres.2012.09.023.

Habicht, K.S., Gade, M., Thamdrup, B., Berg, P., and Canfield, D.E., 2002, Calibration of sulfate levels in the Archean ocean: Science, v. 298, doi:10.1126/science.1078265.

Halverson, G.P., Wade, B.P., Hurtgen, M.T., and Barovich, K.M., 2010, Neoproterozoic chemostratigraphy: Precambrian Research, v. 182, doi:10.1016/j.precamres.2010.04.007.

Holland, H.D., 2006, The oxygenation of the atmosphere and oceans: Philosophical Transactions of the Royal Society B: Biological Sciences, v. 361, doi:10.1098/rstb.2006.1838.

Huh, Y., Chan, L.H., Zhang, L., and Edmond, J.M., 1998, Lithium and its isotopes in major world rivers: implications for weathering and the oceanic budget: Geochimica et Cosmochimica Acta, v. 62, doi:10.1016/S0016-7037(98)00126-4.

Isson, T.T., and Planavsky, N.J., 2018, Reverse weathering as a long-term stabilizer of marine pH and planetary climate: Nature, v. 560, doi:10.1038/s41586-018-0408-4.

Javaux, E.J., and Knoll, A.H., 2017, Micropaleontology of the lower Mesoproterozoic Roper Group, Australia, and implications for early eukaryotic evolution: Journal of Paleontology, v. 91, doi:10.1017/jpa.2016.124.

Jeffcoate, A.B., Elliott, T., Thomas, A., and Bouman, C., 2004, Precise, small sample size determinations of lithium isotopic compositions of geological reference materials and modern seawater by MC-ICP-MS: Geostandards and Geoanalytical Research, v. 28, doi:10.1111/j.1751-908X.2004.tb01053.x.

Kalderon-Asael, B. et al., 2021, A lithium-isotope perspective on the evolution of carbon and silicon cycles: Nature, v. 595, doi:10.1038/s41586-021-03612-1.

Krause, A.J., Sluijs, A., van der Ploeg, R., Lenton, T.M., and Pogge von Strandmann, P.A.E., 2023, Enhanced clay formation key in sustaining the Middle Eocene Climatic Optimum: Nature Geoscience, v. 16, doi:10.1038/s41561-023-01234-y.

Krissansen-Totton, J., and Catling, D.C. A coupled carbon-silicon cycle model over Earth history: Reverse weathering as a possible explanation of a warm mid-Proterozoic climate: Earth and Planetary Science Letters, v. 537, doi:10.1016/j.epsl.2020.116181.

Kuznetsov, A.B., Semikhatov, M.A., and Gorokhov, I.M., 2012, The Sr isotope composition of the world ocean, marginal and inland seas: Implications for the Sr isotope stratigraphy: Stratigraphy and Geological Correlation, v. 20, doi:10.1134/S0869593812060044.

Liu, C.Y., Pogge von Strandmann, P.A.E., Tarbuck, G., and Wilson, D.J., 2022a, Experimental Investigation of Oxide Leaching Methods for Li Isotopes: Geostandards and Geoanalytical Research, v. 46, doi:10.1111/ggr.12441.

Liu, G., Zhang, S., Li, H., Bao, X., Zhao, H., Liang, D., Wu, H., Tang, D., Zhu, X., and Yang, T., 2022b, Cyclostratigraphic calibration of the ca. 1.56 Ga carbon isotope excursion and oxygenation event recorded in the Gaoyuzhuang Formation, north China: Global and Planetary Change, v. 216, doi:10.1016/j.gloplacha.2022.103916.

Lu, S., Yang, C., Li, H., and Li, H., 2002, A Group of Rifting Events in the Terminal Paleoproterozoic in the North China Craton: Gondwana Research, v. 5, doi:10.1016/s1342-937x(05)70896-0.

Luo, J., Long, X., Bowyer, F., and Poulton, S., 2020, Pulsed Oxygenation Events Preceded Progressive Oxygenation of the Early Mesoproterozoic Ocean: Earth and Planetary Science Letters, v. 559, p. 1656–1656, doi:10.46427/gold2020.1656.

Magna, T., Wiechert, U.H., and Halliday, A.N., 2004, Low-blank isotope ratio measurement of small samples of lithium using multiple-collector ICPMS: International Journal of Mass Spectrometry, v. 239, doi:10.1016/j.ijms.2004.09.008.

Marriott, C.S., Henderson, G.M., Crompton, R., Staubwasser, M., and Shaw, S., 2004, Effect of mineralogy, salinity, and temperature on Li/Ca and Li isotope composition of calcium carbonate: Chemical Geology, v. 212, doi:10.1016/j.chemgeo.2004.08.002.

McArthur, J.M., 1994, Recent trends in strontium isotope stratigraphy: Terra Nova, v. 6, doi:10.1111/j.1365-3121.1994.tb00507.x.

Mei, M., 2006, Origin of Molar-Tooth Structure Based on Sequence-Stratigraphic Position and Macroscopic Features: Example from Mesoproterozoic Gaoyuzhuang Formation at Jixian Section, Tianjin, North China: Journal of China University of Geosciences, v. 17, doi:10.1016/S1002-0705(06)60029-0.

Mills, D.B., Ward, L.M., Jones, C.A., Sweeten, B., Forth, M., Treusch, A.H., and Canfield, D.E., 2014, Oxygen requirements of the earliest animals: Proceedings of the National Academy of Sciences of the United States of America, v. 111, doi:10.1073/pnas.1400547111.

Misra, S., and Froelich, P.N., 2012, Lithium isotope history of cenozoic seawater: Changes in silicate weathering and reverse weathering: Science, v. 335, p. 818–823, doi:10.1126/science.1214697.

Nana Yobo, L., Brandon, A.D., Holmden, C., Lau, K. V., and Eldrett, J., 2021, Changing inputs of continental and submarine weathering sources of Sr to the oceans during OAE 2: Geochimica et Cosmochimica Acta, v. 303, doi:10.1016/j.gca.2021.03.013.

Peucker-Ehrenbrink, B., and Fiske, G.J., 2019, A continental perspective of the seawater 87Sr/86 Sr record: A review: Chemical Geology, v. 510, p. 140–165, doi:10.1016/j.chemgeo.2019.01.017.

Pogge von Strandmann, P.A.E., Dellinger, M., and West, A.J., 2021a, Lithium Isotopes: A Tracer of Past and Present Silicate Weathering: Elements in Geochemical Tracers in Earth System Science.

Pogge von Strandmann, P.A.E., Fraser, W.T., Hammond, S.J., Tarbuck, G., Wood, I.G., Oelkers, E.H., and Murphy, M.J., 2019, Experimental determination of Li isotope behaviour during basalt weathering: Chemical Geology, v. 517, doi:10.1016/j.chemgeo.2019.04.020.

Pogge von Strandmann, P.A.E., and Henderson, G.M., 2015, The Li isotope response to mountain uplift: Geology, v. 43, p. 67–70, doi:10.1130/G36162.1.

Pogge von Strandmann, P.A.E., Jenkyns, H.C., and Woodfine, R.G., 2013, Lithium isotope evidence for enhanced weathering during Oceanic Anoxic Event 2: Nature Geoscience, v. 6, doi:10.1038/ngeo1875.

Pogge von Strandmann, P.A.E., Jones, M.T., Joshua West, A., Murphy, M.J., Stokke, E.W., Tarbuck, G., Wilson, D.J., Pearce, C.R., and Schmidt, D.N., 2021b, Lithium isotope evidence for enhanced weathering and erosion during the Paleocene-Eocene Thermal Maximum: Science Advances, v. 7, doi:10.1126/sciadv.abh4224.

Pogge von Strandmann, P.A.E., Schmidt, D.N., Planavsky, N.J., Wei, G., Todd, C.L., and Baumann, K.H., 2019, Assessing bulk carbonates as archives for seawater Li isotope ratios: Chemical Geology, v. 530, p. 119338, doi:10.1016/j.chemgeo.2019.119338.

Poulton, S.W., and Canfeld, D.E., 2011, Ferruginous conditions: A dominant feature of the ocean through Earth's history: Elements, v. 7, doi:10.2113/gselements.7.2.107.

Pourteau, A., Smit, M.A., Li, Z.X., Collins, W.J., Nordsvan, A.R., Volante, S., and Li, J., 2018, 1.6 Ga crustal thickening along the final Nuna suture: Geology, v. 46, p. 959–962, doi:10.1130/G45198.1.

Richter, F.M., Rowley, D.B., and DePaolo, D.J., 1992, Sr isotope evolution of seawater: the role of tectonics: Earth and Planetary Science Letters, v. 109, p. 11–23, doi:10.1016/0012-821X(92)90070-C.

Richter, F.M., and Turekian, K.K., 1993, Simple models for the geochemical response of the ocean to climatic and tectonic forcing: Earth and Planetary Science Letters, v. 119, doi:10.1016/0012-821X(93)90010-7.

Rothman, D.H., Hayes, J.M., and Summons, R.E., 2003, Dynamics of the Neoproterozoic carbon cycle: Proceedings of the National Academy of Sciences of the United States of America, doi:10.1073/pnas.0832439100.

Sahoo, S.K., Planavsky, N.J., Kendall, B., Wang, X., Shi, X., Scott, C., Anbar, A.D., Lyons, T.W., and Jiang, G., 2012, Ocean oxygenation in the wake of the Marinoan glaciation: Nature, v. 489, doi:10.1038/nature11445.

Shang, M., Tang, D., Shi, X., Zhou, L., Zhou, X., Song, H., and Jiang, G., 2019, A pulse of oxygen increase in the early Mesoproterozoic ocean at ca. 1.57–1.56 Ga: Earth and Planetary Science Letters, v. 527, p. 115797, doi:10.1016/j.epsl.2019.115797.

Shi, W., Mills, B.J.W., Li, C., Poulton, S.W., Krause, A.J., He, T., Zhou, Y., Cheng, M., and Shields, G.A., 2022, Decoupled oxygenation of the Ediacaran ocean and atmosphere during the rise of early animals: Earth and Planetary Science Letters, v. 591, doi:10.1016/j.epsl.2022.117619.

Shields, G.A., Mills, B.J.W., Zhu, M., Raub, T.D., Daines, S.J., and Lenton, T.M., 2019, Unique Neoproterozoic carbon isotope excursions sustained by coupled evaporite dissolution and pyrite burial: Nature Geoscience, v. 12, p. 823–827, doi:10.1038/s41561-019-0434-3.

Spooner, E.T.C., 1976, The strontium isotopic composition of seawater, and seawater-oceanic crust interaction: Earth and Planetary Science Letters, v. 31, doi:10.1016/0012-821X(76)90108-4.

Tang, D. et al., 2022, Enhanced Weathering Triggered the Transient Oxygenation Event at ~1.57 Ga: Geophysical Research Letters, v. 49, doi:10.1029/2022GL099018.

Teixeira, W., Reis, N.J., Bettencourt, J.S., Klein, E.L., and Oliveira, D.C., 2019, Intraplate proterozoic magmatism in the amazonian craton reviewed: Geochronology, crustal tectonics and global barcode matches, *in* Springer Geology, doi:10.1007/978-981-13-1666-1_4.

Tessier, A., Campbell, P.G.C., and Bisson, M., 1979, Sequential Extraction Procedure for the Speciation of Particulate Trace Metals: Analytical Chemistry, v. 51, doi:10.1021/ac50043a017.

Turgeon, S.C., and Creaser, R.A., 2008, Cretaceous oceanic anoxic event 2 triggered by a massive magmatic episode: Nature, v. 454, doi:10.1038/nature07076.

Walker, J.C.G., Hays, P.B., and Kasting, J.F., 1981, A negative feedback mechanism for the long-term stabilization of Earth's surface temperature.: Journal of Geophysical Research, 86, doi:10.1029/JC086iC10p09776.

Weis, D. et al., 2006, High-precision isotopic characterization of USGS reference materials by TIMS and MC-ICP-MS: Geochemistry, Geophysics, Geosystems, v. 7, doi:10.1029/2006GC001283.

West, A.J., Galy, A., and Bickle, M., 2005, Tectonic and climatic controls on silicate weathering: Earth and Planetary Science Letters, v. 235, doi:10.1016/j.epsl.2005.03.020.

Xie, B., Zhu, J. ming, Wang, X., Xu, D., Zhou, L., Zhou, X., Shi, X., and Tang, D., 2023, Mesoproterozoic oxygenation event: From shallow marine to atmosphere: Bulletin of the Geological Society of America, v. 135, doi:10.1130/B36407.1.

Xu, D., Qin, Z., Wang, X., Li, J., Shi, X., Tang, D., and Liu, J., 2023, Extensive sea-floor oxygenation during the early Mesoproterozoic: Geochimica et Cosmochimica Acta, v. 354, doi:10.1016/j.gca.2023.06.007.

Zhang, T., Li, M., Chen, X., Wang, T., and Shen, Y., 2022, High atmospheric CO2 levels in the early Mesoproterozoic estimated from paired carbon isotopic records from carbonates from North China: Precambrian Research, v. 380, doi:10.1016/j.precamres.2022.106812.

Zhang, S., Li, Z.X., Evans, D.A.D., Wu, H., Li, H., and Dong, J., 2012a, Pre-Rodinia supercontinent Nuna shaping up: A global synthesis with new paleomagnetic results from North China: Earth and Planetary Science Letters, v. 353–354, doi:10.1016/j.epsl.2012.07.034.

Zhang, S.H., Zhao, Y., and Santosh, M., 2012b, Mid-Mesoproterozoic bimodal magmatic rocks in the northern North China craton: Implications for magmatism related to breakup of the columbia supercontinent: Precambrian Research, v. 222–223, p. 339–367, doi:10.1016/j.precamres.2011.06.003.

Zhang, K., Zhu, X., Wood, R.A., Shi, Y., Gao, Z., and Poulton, S.W., 2018, Oxygenation of the Mesoproterozoic ocean and the evolution of complex eukaryotes: Nature Geoscience, v. 11, p. 345–350, doi:10.1038/s41561-018-0111-y.

Zhu, S., Zhu, M., Knoll, A.H., Yin, Z., Zhao, F., Sun, S., Qu, Y., Shi, M., and Liu, H., 2016, Decimetre-scale multicellular eukaryotes from the 1.56-billion-year-old Gaoyuzhuang Formation in North China: Nature Communications, v. 7, doi:10.1038/ncomms11500.

Acknowledgments

We appreciate D. Wilson and T. Gernon for valuable suggestions, and C. Liu, X. Liu and W. Shi for helpful discussions.

Funding: This study was supported from the Natural Environment Research Council (NERC) (NE/P013643/1 (BETR programme) to G.A.S., Y.Z. and S.W.P.; and NE/R010129/1 to G.A.S., S.W.P. and P.A.E.P.v.S); the National Key Research and Development Program of China (2022YFF0800100); the National Natural Science Foundation of China (41921002) to M.Z.; and the Dean's Prize of the Faculty of Mathematical and Physical Sciences (UCL) to X.C.

Author contributions: X.C., Y.Z., and G.A.S. conceived and designed the study. X.C. and Y.Z. developed the methodology. F.T.B., C.M., S.Z., M.Z., and D.L. carried out the investigation and data collection. X.C. and F.T.B. prepared the visualizations. Y.Z. and G.A.S. supervised the research. X.C. wrote the original draft of the manuscript. All authors contributed to reviewing and editing the manuscript, including X.C., Y.Z., S.W.P., F.T.B., C.M., S.Z., M.Z., D.L., P.A.E.P.v.S., B.J.W.M., and G.A.S.

Competing interests: Authors declare that they have no competing interests.

574 **Figures**

575

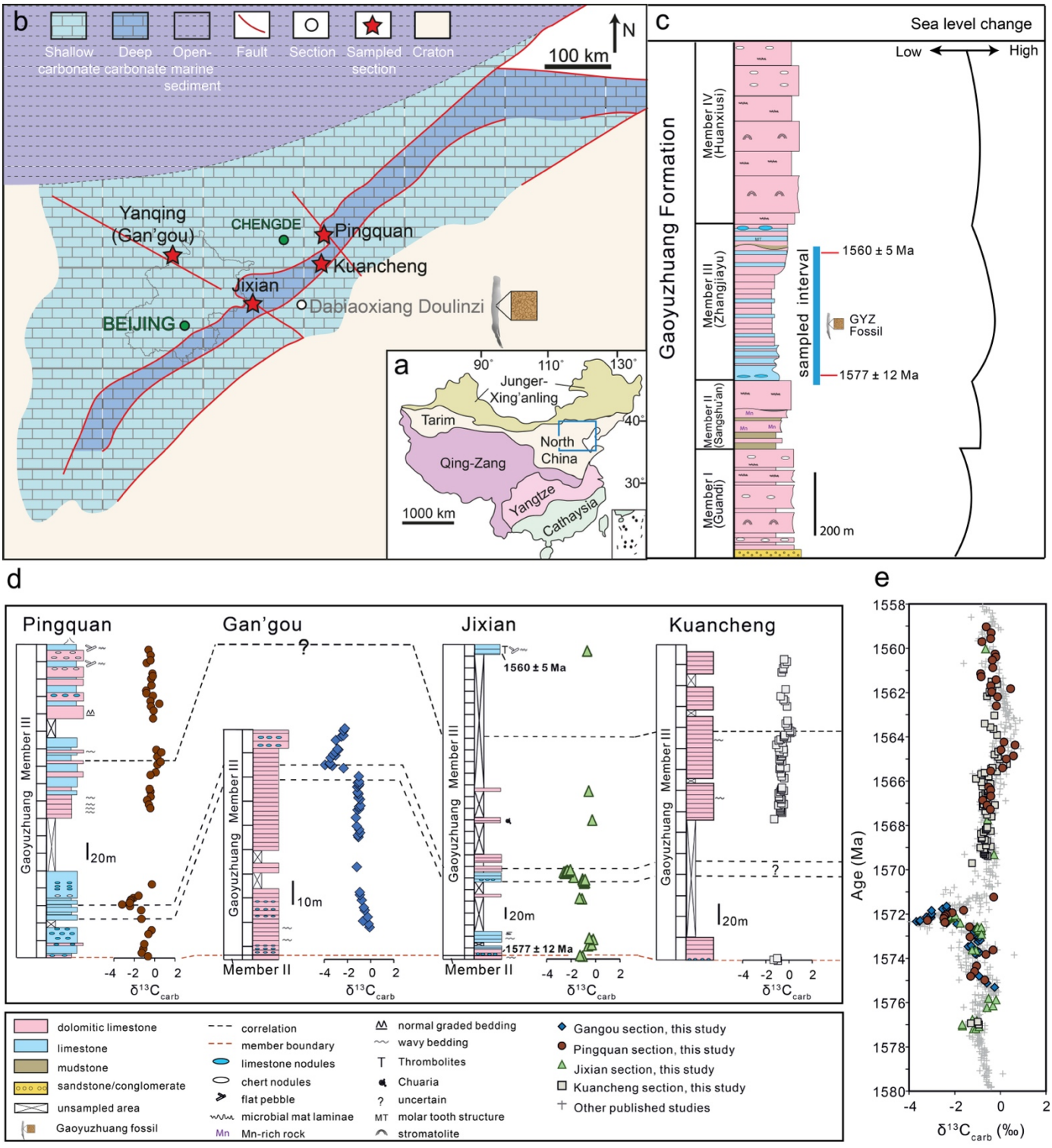

Figure 1. Geological background of the study area. (a) Major tectonic subdivisions of China, modified after (Shang et al., 2019). The blue box shows the area of panel b (Yanliao Basin, North China). (b) Simplified

Mesoproterozoic paleogeographic map of North China during deposition of the Gaoyuzhuang Formation. The four sampling sections are Jixian (40°9'21.77"N, 117°28'39.69"E), Kuancheng (40°36'14.02"N, 118°31'31.75"E), Gangou (40°39'49"N, 116°14'30"E) and Pingquan (40°57'48"N, 118°36'25"E). (c) General stratigraphic columns of Gaoyuzhuang Formation and sea level change (modified from Zhang et al., 2018). (d) Carbon isotope correlation for Gaoyuzhuang Member III across the four sections analysed in this study. (e) Age model for Gaoyuzhuang Member III (and part of Member II) in relation to $\delta^{13}C_{carb}$ data from this study and other published studies (Guo et al., 2013; Zhang et al., 2018; Shang et al., 2019) (shown as grey crosses). Errors are smaller than the symbols used.

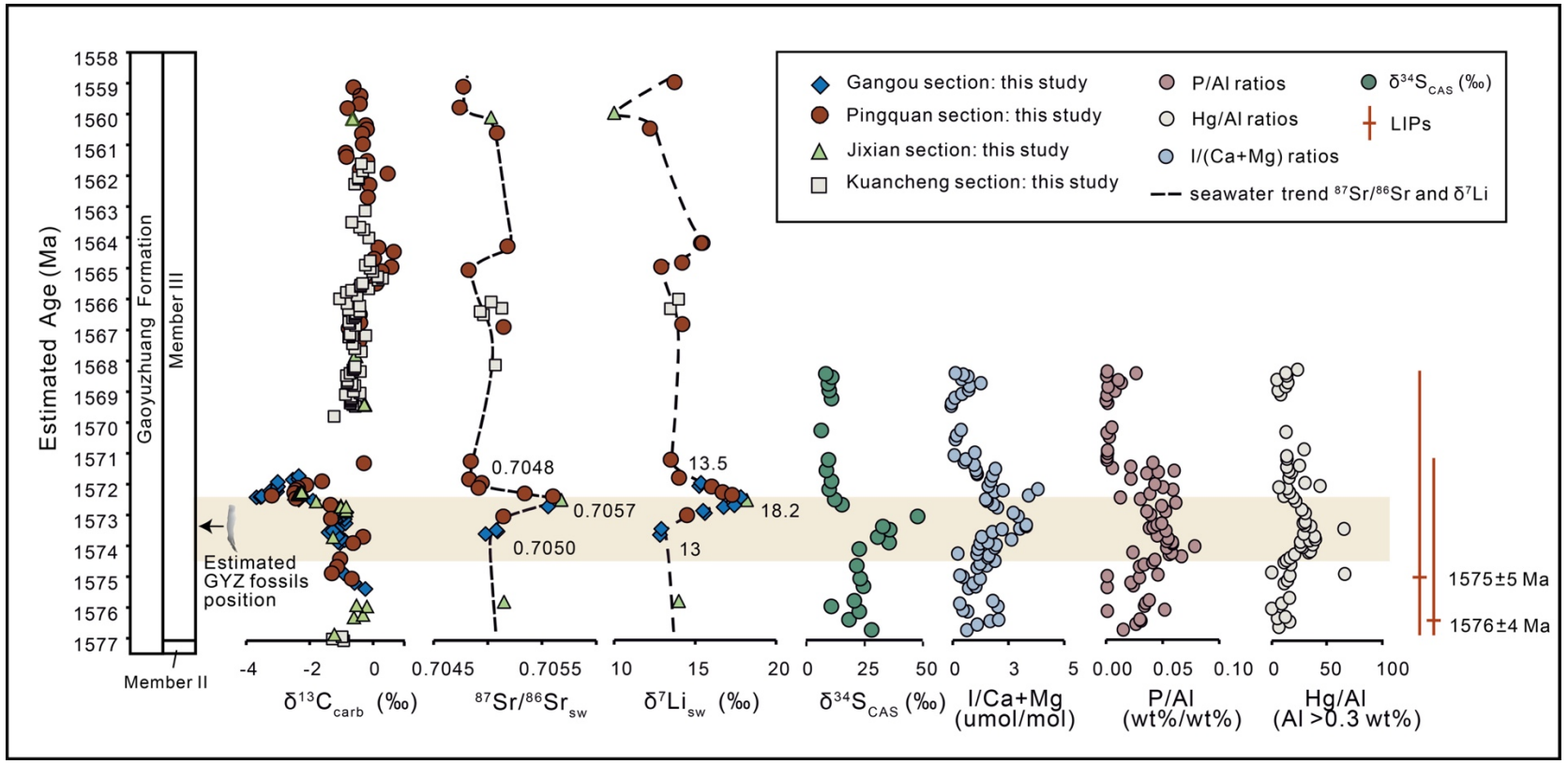

Figure 2. Geochemical profiles through Gaoyuzhuang Formation Member III. C, Sr and Li isotopes are from the four sections (Gangou, Jixian, Pingquan, Kuancheng) of this study. An average fractionation factor (5‰) has been applied to the δ^7Li profile to estimate seawater values (see Supplementary Information for details). A coupled positive excursion in seawater Sr and Li isotopes correlates to the negative C isotope excursion (shown by the yellow band). $\delta^{34}S_{CAS}$, I/(Ca + Mg), P/Al and Hg/Al are from published studies of the Gangou section (Shang et al., 2019; Tang et al., 2022; Xie et al., 2023). Intensified volcanic activity is evidenced by

large igneous provinces (LIPs), such as in Amazonia (1576 ± 4 Ma; Teixeira et al., 2019) and West Africa (1575 ± 5 Ma; Teixeira et al., 2019). Slight differences in the starting points of $\delta^{34}S_{CAS}$, I/Ca+Mg, P/Al, and Hg/Al (from other studies) compared to Sr and Li isotopes (this study) may result from uncertainties in stratigraphic correlation. Analytical uncertainties are smaller than the size of the symbols.

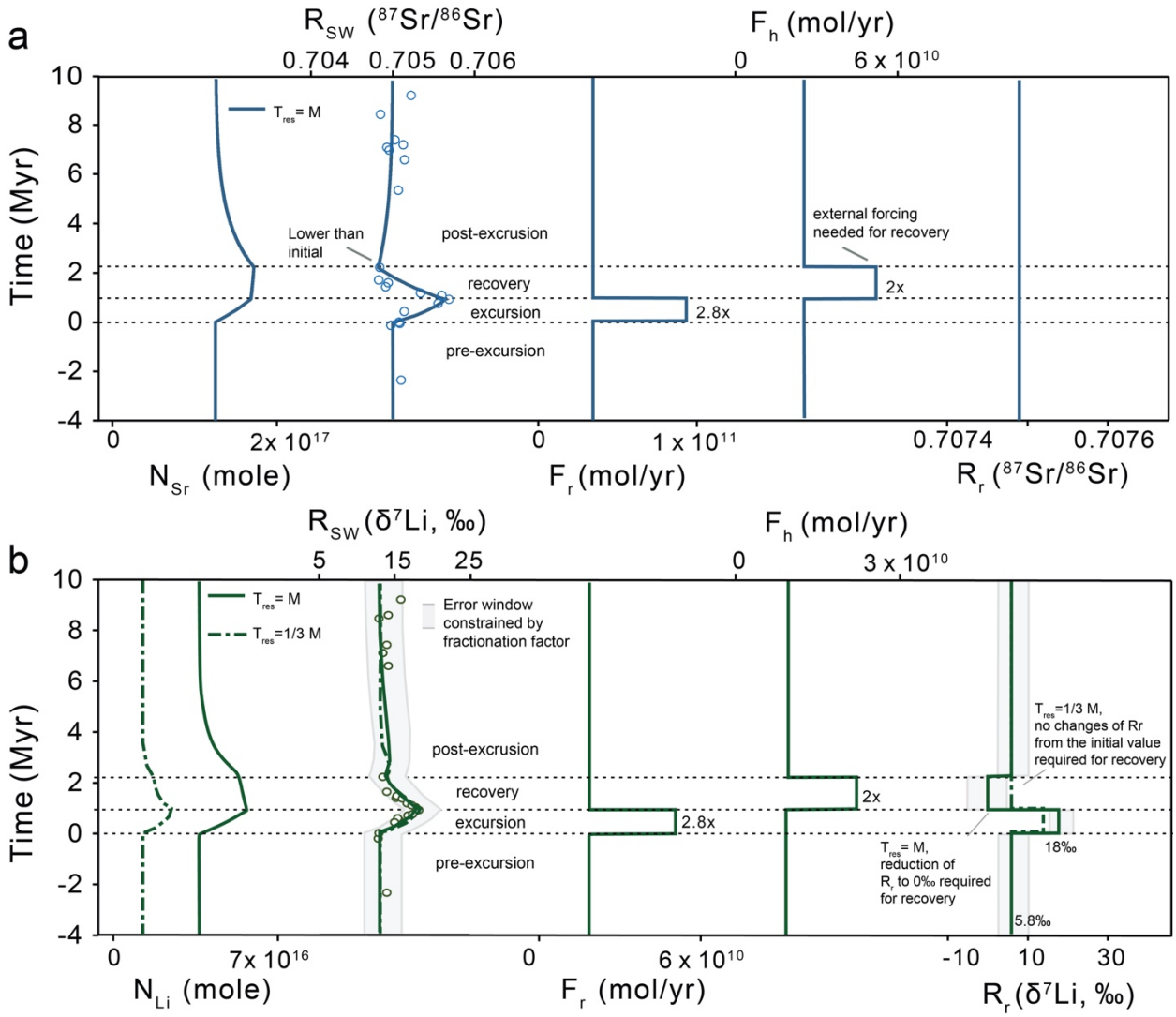

Figure 3. Modelling results for the observed seawater Sr and Li isotope excursions. a) Modelling results for Sr isotopes. Given the modern residence time and an unchanged riverine input value (R_r), a 2.8 times increase in continental weathering flux (F_r) and a 2 times increase in hydrothermal input (F_h) are required to account for the increasing and decreasing trends, respectively. Blue circles represent measured Sr isotope values. **b)** Modelling results for Li isotopes. Times of increases for F_r and F_h are constrained by Sr isotopes with modern residence time. The grey band indicates the modelled error window constrained by the full range of fractionation factors (3–8.5‰; Marriott et al., 2004; Pogge von Strandmann et al., 2013; Pogge von Strandmann et al., 2019; Day et al., 2021; Krause et al., 2023) during Li incorporation into carbonates. Green circles represent seawater Li isotope values estimated from measured rock values by adding the mean fractionation factor (5‰), and green lines represent model outputs using the mean fractionation factor. The

solid line shows results based on the modern residence time, while the dashed line reflects results with a reduced residence time. Given the modern residence time, an ~12‰ (full range 10–13‰) increase from the initial value and a decrease to 0‰ (-5–5‰) in riverine δ^7Li (R_r) are required to achieve the observed increasing and decreasing trends. A reduced residence time requires a lower riverine δ^7Li ($R_{r\text{-}Li}$) composition to achieve the peak value, and leads to a rapid recovery without an additional decrease in riverine δ^7Li (green dash lines). A reduced residence time for Li isotopes is likely, considering increased marine reverse weathering in the Precambrian, but this is not applicable for Sr isotopes. More sensitivity tests on the residence time are provided in the Supplementary Information. T_{res}: residence time; M: modern residence time; N: total inventory of the seawater reservoir; R: isotopic ratio; F: flux; sw: seawater; r: river; h: hydrothermal. Analytical uncertainties are smaller than the size of the symbols.

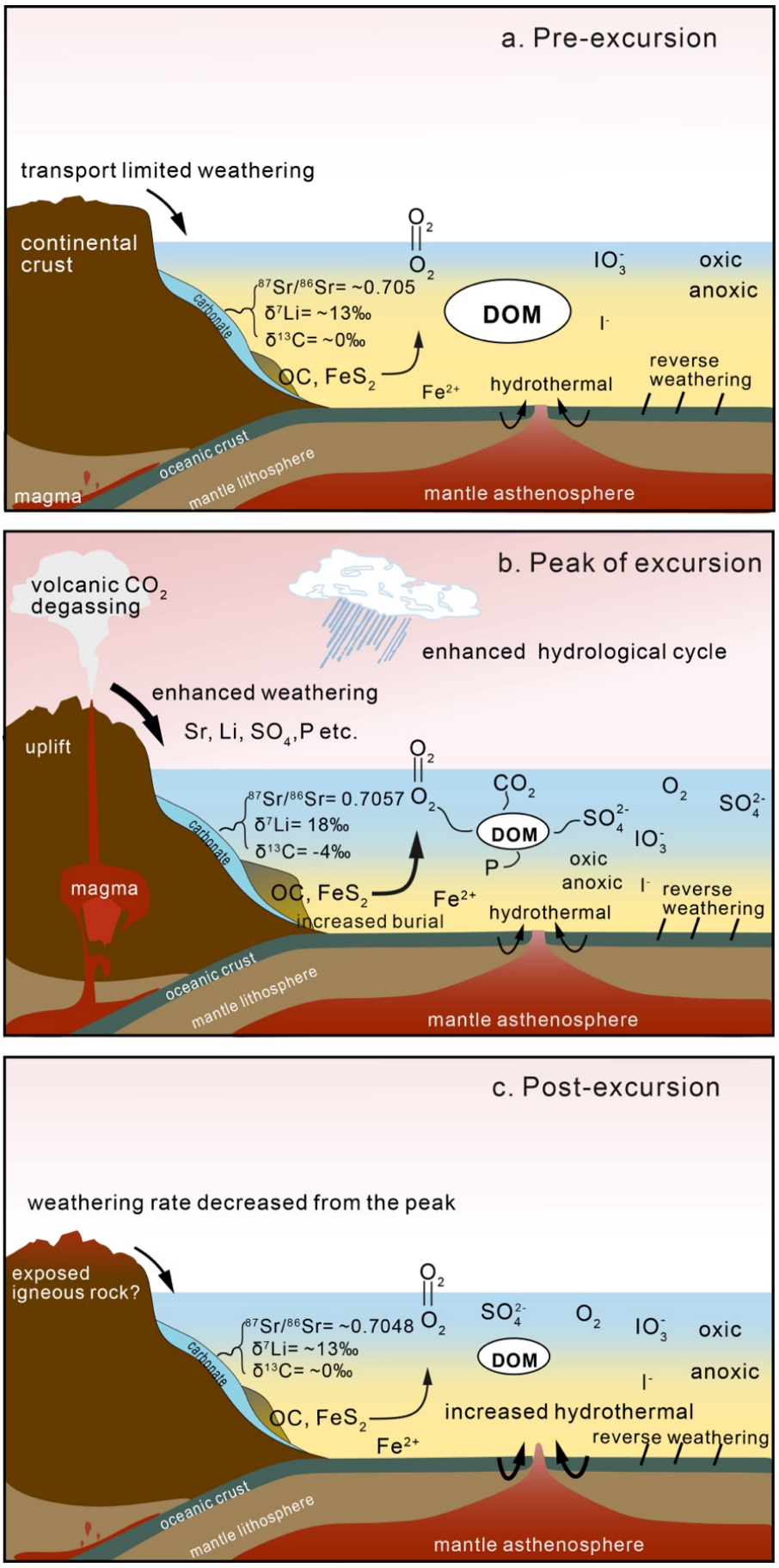
a. Pre-excursion
transport limited weathering
continental crust
O_2
O_2
IO_3^-
oxic
anoxic
$^{87}Sr/^{86}Sr$= ~0.705
δ^7Li= ~13‰
δ^{13}C= ~0‰
carbonate
DOM
I^-
OC, FeS_2
Fe^{2+}
hydrothermal
reverse weathering
oceanic crust
mantle lithosphere
magma
mantle asthenosphere
b. Peak of excursion
volcanic CO_2 degassing
enhanced hydrological cycle
enhanced weathering
Sr, Li, SO_4,P etc.
uplift
O_2
O_2
CO_2
O_2
SO_4^{2-}
$^{87}Sr/^{86}Sr$= 0.7057
δ^7Li= 18‰
δ^{13}C= -4‰
carbonate
DOM
SO_4^{2-}
IO_3^-
P
oxic
anoxic
I^-
magma
OC, FeS_2
Fe^{2+}
reverse weathering
increased burial
hydrothermal
oceanic crust
mantle lithosphere
mantle asthenosphere
c. Post-excursion
weathering rate decreased from the peak
exposed igneous rock?
O_2
O_2
SO_4^{2-}
O_2
IO_3^-
oxic
$^{87}Sr/^{86}Sr$= ~0.7048
δ^7Li= ~13‰
δ^{13}C= ~0‰
carbonate
DOM
I^-
anoxic
OC, FeS_2
Fe^{2+}
increased hydrothermal
reverse weathering
oceanic crust
mantle lithosphere
mantle asthenosphere

Figure 4. Conceptual model linking the weathering event to carbon cycle perturbation and marine oxygenation. The arrow width represents the relative magnitude of each flux. **a)** Prior to the Sr and Li isotope excursion. The general Mesoproterozoic climate was warm, and weathering regime was transport-limited, accompanied by low sulfate and nutrient inputs, with a prominent level of ocean anoxia. **b)** The peak of the Sr and Li isotope excursion. Increased volcanic degassing, coupled with accretional orogenic uplift, triggered an enhanced weathering rate with more secondary mineral formation (incongruent weathering), resulting in an increase in seawater Sr and Li isotope values. Elevated sulfate and nutrient inputs led to enhanced productivity and pyrite burial, potentially raising oxygen levels. The increased availability of marine oxidants (O_2 and SO_4) oxidized dissolved organic matter (DOM) and drove the carbon isotope excursion. DOM oxidation likely further released CO_2 and P, sustaining the weathering. **c)** After the Sr and Li isotope excursion. Cessation of DOM oxidation and reduced weathering gradually returned Sr, Li and C isotope values to their initial state, and prompted a return of widespread oceanic anoxia. The lower Sr isotope value compared to the initial state may potentially be attributed to an increased hydrothermal flux, possibly in conjunction with greater exposure of relatively unradiogenic igneous rock.

Supplementary Materials for

Enhanced weathering and its potential connection to ocean oxygenation and eukaryotic evolution at 1.57 Ga

Xi Chen[1,2]*, Ying Zhou[1,3], Simon W. Poulton[4], Fred T. Bowyer[5], Colin Mettam[1], Shihong Zhang[6], Maoyan Zhu[7,8], Da Li[9], Philip A.E. Pogge von Strandmann[1,3], Benjamin J. W. Mills[4], Graham A. Shields[1]

[1] LOGIC, Department of Earth Sciences, University College London, London, UK

[2] School of Ocean and Earth Science, University of Southampton, Southampton, UK.

[3] MIGHTY, Institute of Geosciences, Johannes Gutenberg University, Mainz, Germany

[4] School of Earth and Environment, University of Leeds, Leeds LS2 9JT, UK

[5] School of Geosciences, University of Edinburgh, Edinburgh, UK

[6] State key Laboratory of Biogeology and Environmental Geology, China University of Geosciences, Beijing, China

[7] State Key Laboratory of Palaeobiology and Stratigraphy, Nanjing Institute of Geology and Palaeontology, Chinese Academy of Sciences, Nanjing, China

[8] College of Earth and Planetary Sciences, University of Chinese Academy of Sciences, Beijing, China

[9] School of Marine Science and Engineering, Nanjing Normal University, Nanjing, China

*Corresponding author. Email: Xi.Chen@soton.ac.uk

This PDF file includes:

Supplementary Text

1. Correlation and age model

Inorganic carbon isotopes ($\delta^{13}C_{carb}$) are typically resistant to diagenesis due to the relatively low water/rock ratio for carbon during interactions with diagenetic and post-diagenetic fluids. The negative carbon isotope excursion in the Gaoyuzhuang Formation has been extensively studied and is considered a primary seawater signal (Zhang et al., 2018; Shang et al., 2019). In our analysis, we plotted the $\delta^{13}C_{carb}$ values from the four sections relative to diagenetic and clay contamination indicators (**Fig. S1**). The results reveal that there is no significant correlation observed for any of the indices across all sections (Mg/Ca, Mn/Sr, Sr/Ca+Mg, $^{87}Sr/^{86}Sr$, $\delta^{18}O_{carb}$, Al/Ca), except for a Mn-rich dolomitic limestone in the Jixian section. The Mn-rich dolomitic limestone observed in the Jixian section exhibits a negative correlation with $\delta^{13}C_{carb}$ values during this period. This relationship has been proposed to be a consequence of marine oxygenation, where intermittent oxygenation events led to the oxidation of dissolved Mn (II) in the water column to insoluble Mn (IV), followed by partial reduction to Mn-carbonate during early diagenesis (Fang et al. 2020). In this case, like previous studies, we consider the $\delta^{13}C_{carb}$ data presented in this paper to primarily reflect contemporaneous seawater signatures.

The stratigraphic correlations and age models used in this study were based on carbon isotope stratigraphy. U-Pb zircon dating of tuffs gives absolute age constraints at the top and base of Gaoyuzhuang Member III, with 1560 ± 5 Ma (Li et al., 2010) and ~1577 ± 12 Ma (Tian et al., 2015), respectively. Age tie points were selected at the peak and recovery of $\delta^{13}C$ excursions and the member boundaries. Carbon isotope correlation is based on established lithostratigraphic member subdivision and visual alignment given the currently available level of detail (**Fig. 1d in main text).** For each section, the age model was constructed by linear interpolation between tie points based on the assumption of constant sediment accumulation rates. The duration of the $\delta^{13}C$ excursion fits well the published cyclostratigraphic calibration (Liu et al., 2022). $^{87}Sr/^{86}Sr$ and $\delta^{7}Li$ values for the four sections were integrated using their relative position with respect to the $\delta^{13}C$ anomaly in each section, as well as the overall age model. We further correlate $\delta^{13}C_{carb}$ values from this study with other published studies of Gaoyuzhuang Member III (Guo et al., 2013; Zhang et al., 2018; Shang et al., 2019) **(Fig. 1e in main text).** Proxies such as $\delta^{34}S_{CAS}$, I/(Ca + Mg), P/Al and Hg/Al, measured from samples of these published sections, can consequently be linked to this study **(Fig. 2** in the main text**).**

2. Sample screening and reconstruction of seawater Sr and Li isotope trends

Petrographic features

Strontium and lithium isotopic records in carbonate can be influenced by diagenetic alteration and clay contamination, making it crucial to assess the extent to which these records represent syn-depositional oceanic values. Typical microscopic features associated with their Sr isotopes in four studied sections of Gaoyuzhuang Formation (G: Gangou section; P: Pingquan section; J: Jixian section; K: Kuancheng section) are shown in **Fig. S2.** **Fig. S2a–e** show micritic limestone/dolomitic limestone, which are normally considered as syn-depositional and early diagenetic signals. Samples in f–h, by contrast, show apparently larger grain size, indicating recrystallization. The Kuancheng sample K72 (f) shows detrital material, such as angular quartz grains. Samples from the Gangou section (g, h) are organic-rich with subhedral to euhedral dolomite. Consistently, samples in images f–h contain $^{87}Sr/^{86}Sr$ signals that are significantly higher than contemporary seawater.

Geochemical screening

Diagenetic alteration or clay contamination varies from section to section, and different lithologies also exhibit distinct geochemical features (e.g., dolomite generally exhibits a greater affinity for Fe and Mn and a lower affinity for Sr, compared to calcite) (Vahrenkamp and Swart, 1990). Therefore, examining geochemical data from all sections and all lithologies together may conceal diagenetic or contamination trends in each section/lithology. Based on the bulk Mg/Ca (g/g) ratios, samples from the Pingquan and Jixian sections can be divided into two lithological groups: $Mg/Ca < 0.1$ and $0.2 < Mg/Ca < 0.6$, which are referred to as limestone and dolomitic limestone, respectively. Samples from the Kuancheng and Gangou sections display a more uniform Mg/Ca ratio ($0.2 < Mg/Ca < 0.6$). Following petrographic observation, we used a four-step geochemical screening approach to select the data section-by-section and lithology-by-lithology: 1) diagenesis evaluation; 2) clay contamination evaluation; 3) cut-off validity evaluation; 4) section comparison.

First, we assessed diagenetic alteration by plotting the Mn/Sr, Sr/(Ca+Mg) and Mg/Ca ratios of bulk carbonate against the $^{87}Sr/^{86}Sr$ ratios (**Fig. S3**). The Gangou section and Kuancheng section are characterised by dolomitic limestone (shown in pink). A clear positive correlation is observed between $^{87}Sr/^{86}Sr$ and Mn/Sr ($R^2 = 0.69$) in the Gangou section, while no correlation is observed for the Kuancheng section. The Pingquan and Jixian sections are composed of both limestone (shown in blue) and dolomitic limestone. Mn-enriched dolomitic samples (shown in purple) are further separated from non-Mn enriched dolomitic samples in the Jixian section for the plot of $^{87}Sr/^{86}Sr$ versus Mn/Sr ratios (**Fig. S3**). For limestone samples of the Pingquan and Jixian sections, no correlations are observed among $^{87}Sr/^{86}Sr$ and all three parameters in the Pingquan section, while a strong correlation is observed between $^{87}Sr/^{86}Sr$ and Mn/Sr ($R^2 = 0.88$) for the Jixian section (**Fig. S3**). For dolomitic limestones, a positive correlation between $^{87}Sr/^{86}Sr$ and Mn/Sr ($R^2 = 0.64$) is observed for the Pingquan section. Mn-enriched dolomitic limestones in the Jixian section do not exhibit any correlation with $^{87}Sr/^{86}Sr$ ratios, but their $^{87}Sr/^{86}Sr$ values (> 0.7079) are all significantly higher than contemporaneous seawater (0.705–0.706). It is most likely that Mn-enriched dolomitic limestones have all undergone some degree of diagenetic alteration in terms of Sr isotope ratios. Based on observations and the suggested threshold(Chen and Zhou, 2023) for Gaoyuzhuang samples, cut-offs of Mn/Sr < 2 g/g, Mg/Ca < 0.4 g/g, and Sr/(Ca+Mg) > 200 μg/g were applied for dolomitic limestone samples; Mn/Sr < 1 g/g, Mg/Ca < 0.05 g/g, and Sr/(Ca+Mg) > 200 μg/g were applied for limestone samples. Only samples that satisfy all three criteria were considered in the next step.

Second, for samples that passed diagenetic screening, we examined clay contamination for Li and Sr isotopes separately, considering the different leaching techniques applied for Sr and Li isotopes in this study. We plotted Rb/(Ca+Mg) and Al/(Ca+Mg) in the Li isotope leachate (NaOAc) against δ^7Li, and Rb/Sr and Al/(Ca+Mg) in the Sr leachate (HAc) against $^{87}Sr/^{86}Sr$ (**Fig. S4**). For Sr isotopes, we recommend values of Rb/Sr < 5 mg/g and Al/(Ca +Mg) < 1 mg/g as cut-offs, as samples beyond this threshold generally fall outside the contemporaneous seawater range (~0.705–0.706) (Chen et al., 2022), possibly because of clay mineral contamination. For Li isotopes, all samples have low Rb/(Ca+Mg) values (<15 μg/g), but samples with Al/(Ca+Mg) > 1 mg/g exhibit negative covariation with δ^7Li **(Fig. S4)**, likely indicating detrital contamination as silicate minerals normally contain lower δ^7Li (Dellinger et

al., 2020). To limit potential silicate contamination, similar to Sr isotopes, only samples with Al/(Ca+Mg) < 1 mg/g were deemed acceptable here.

Third, to evaluate the validity of the applied cut-off values, we further plotted $^{87}Sr/^{86}Sr$ and $\delta^{7}Li$ values for all samples that passed the first two steps, against all indicators of diagenesis and detrital contamination discussed above, i.e. Mg/Ca, Sr/(Ca+Mg), Mn/Sr, Rb/(Ca+Mg), Rb/Sr, Li/(Ca+Mg), and Al/(Ca+Mg), alongside $\delta^{18}O$ (**Fig. S5**). For Sr isotope values, samples from the Pingquan, Jixian and Kuancheng sections show no remaining covariation between these indices, and so were used for seawater $^{87}Sr/^{86}Sr$ reconstruction. However, for the Gangou section, covariation of $^{87}Sr/^{86}Sr$ with Sr/(Ca+Mg), Mn/Sr and Mg/Ca are observed, implying that likely diagenetic exchange drove carbonate $^{87}Sr/^{86}Sr$ ratios towards higher values **(Fig. S5).** By contrast, for Li isotopes, no covariation was observed between $\delta^{7}Li$ and alteration indices for any of the sections, which suggests that there is little to no contribution of Li from diagenetic or non-carbonate sources in the selected samples.

Finally, we conducted section comparisons for samples that passed thresholds in the first two steps and then constructed seawater Sr and Li isotope trends associated with observations in step 3. We plotted $^{87}Sr/^{86}Sr$ and $\delta^{7}Li$ values of the samples against stratigraphic level (ages) for each section (**Fig. S6a, S6c**) and in terms of Mg/Ca ratios (limestone and dolomitic limestone; **Fig. S6b, S6d**). In theory, without diagenetic alteration or non-carbonate contamination, open marine carbonates from different sections and lithologies should show similar values at the same stratigraphic level, as the Sr and Li compositions of open seawater are expected to be homogeneous. We find that the Li isotope values of selected samples from the four different sections and different lithologies exhibit similar amplitudes and $\delta^{7}Li$ values within a similar stratigraphic level (especially for samples encompassing the positive excursion), which confirms the validity of our screening approach. For Sr isotopes, the selected samples from the Pingquan, Jixian and Kuancheng sections exhibit little difference at a similar stratigraphic level, suggesting robust seawater values. However, samples from the Gangou section (dolomitic limestone) display higher peak values in $^{87}Sr/^{86}Sr$ ratios compared to other sections (Pingquan and Jixian sections, mainly limestones), which is consistent with the diagenetic trends observed in step 3 (**Fig. S5)**, indicating a strong likelihood of diagenetic alteration/dolomitization. Thus, for the Gangou section, only the lowest values (diagenesis increases $^{87}Sr/^{86}Sr$ values in this study) that

are comparable to the values in the other three sections at the same stratigraphic level can be considered to approximate seawater values.

Reconstruction of seawater Sr and Li isotope trends

Based on the above observations, to reconstruct the seawater evolution trend for Sr isotopes, we primarily used screened samples from the Jixian, Pingquan and Kuancheng sections, and only incorporated samples from the Gangou section when the lowest values are comparable to correlative, unaltered samples from other sections. The seawater $^{87}Sr/^{86}Sr$ values in this study range from 0.70483 to 0.70569, which are within the range of published 1.6–1.4 Ga seawater values (~0.7046–0.7058) (Chen et al., 2022; Gorokhov et al., 2022).

For Li isotopes, a fractionation factor needs to be applied to measured δ^7Li values because ^6Li is preferentially incorporated into carbonate rocks during precipitation (Marriott et al., 2004). The fractionation factor for carbonate δ^7Li depends on the original mineralogy (calcite or aragonite) and the type of diagenesis (fluid-buffered or sediment-buffered). Inorganic calcite precipitation is associated with a fractionation factor ($\Delta_{sw\text{-}calcite}$) ranging from 3–8.5‰ (Marriott et al., 2004; Pogge von Strandmann et al., 2017, 2019; Dellinger et al., 2018; Day et al., 2021). Aragonite precipitation exhibits a slightly larger fractionation factor ($\Delta_{sw\text{-}aragonite}$) of around 10‰ (Dellinger et al., 2018; Pogge von Strandmann et al., 2019; Day et al., 2021). The Li isotope fractionation that occurs during dolomite formation is not well understood at present, but some research shows that the dolomite fractionation factor is similar to the calcite (Liu et al., 2023). The Li isotope value captured by carbonate also depends on whether the system is rock-buffered or fluid-buffered during marine diagenesis. During sediment-buffered (closed) diagenesis, the composition of the precipitated carbonate reflects the chemical composition of the primary mineralogy (aragonite or calcite). Conversely, during fluid-buffered (open) diagenesis, the δ^7Li of carbonate reflects the chemical composition of the diagenetic fluid (Higgins et al., 2018; Dellinger et al., 2020).

Fully interpreting the original mineralogy and diagenetic types based on available data from this study is challenging. However, we have observed similar δ^7Li values in different lithologies (limestone and dolomitic limestone) at the same stratigraphic level (**Fig. S6**). Based on previous studies, this could result from a few different scenarios. First, both limestone and dolomitic

samples may have undergone fluid-buffered diagenesis in seawater conditions, which results in similar values close to seawater composition (Dellinger et al., 2020; Crockford et al., 2021; Murphy et al., 2022). It has been proposed that marine low-magnesium calcite and dolomite formed under fluid-buffered conditions have compositions similar to marine pore waters and consistently exhibit δ^7Li values that reliably record seawater composition during the time of diagenetic alteration ($\Delta_{sw\text{-}carb}$ ~0.5–1.5 ‰; ref. *83*).

Second, limestone and dolomitic limestone could also have experienced sediment-buffered diagenesis, preserving the δ^7Li signature of the original mineralogy (calcite or aragonite). However, we question the validity of the above two scenarios, as Sr isotope values of the same set of samples are quite different. Third, the transition from the original mineralogy to dolomite might involve a similar fractionation factor as that occurring in the shift from the original mineralogy to low-Mg calcite. This could explain why the dolomite samples, despite exhibiting higher Sr isotopic values compared to the low-Mg calcite samples, have similar Li isotope values to the low-Mg calcite samples (**Fig. S6a, 6b**). However, this cannot be confirmed without more evidence from dolomite synthesis experiments. Last, but not least, even though the bulk carbonate Mg/Ca ratios show two different lithology groups, the leachate Mg/Ca values are consistently below 0.1 g/g. This suggests that the phases we dissolved for δ^7Li measurements primarily comprise the calcite fraction, as dolomite and aragonite are more difficult to dissolve using weak acid or *p*H buffered solution compared to calcite. It is likely that the measured δ^7Li values for both limestone and dolomitic limestone are associated with the primary calcite fraction of the samples, and this is supported also by the lack of clear correlation with diagenetic indicators (**Fig. S5**), thus, no difference can be observed for various lithologies.

Although confirmation of the hypotheses would benefit from additional evidence, such as the pairing of calcium and magnesium isotopes ($\delta^{44/40}$Ca, δ^{26}Mg) (Crockford et al., 2021; Murphy et al., 2022), the similarity in δ^7Li values between the two lithologies suggests that a single fractionation factor can be convincingly applied to obtain an estimate of the seawater value. Considering samples in this study have Sr/Ca ratios much lower than for pristine modern aragonite (10 mmol/mol), here we apply an average calcite fractionation factor (~5‰) to all samples to estimate the seawater value (Pogge von Strandmann et al., 2013). The full range of fractionation factors (~3–8.5‰) is used in the model to constrain the error window.

Similar to Sr isotope values, the reconstructed seawater δ^7Li values (~10‰– ~18‰) are also close to the range of compiled 1.6–1.4 Ga seawater values (~5‰–20‰) (Kalderon-Asael et al., 2021). The combination of petrographic and multi-step geochemical screening used in this study demonstrates the robustness of our reconstructed seawater δ^7Li and $^{87}Sr/^{86}Sr$ records, and the reliability of the coupled Sr and Li positive isotope excursion**.**

3. Modelling the Sr and Li isotope positive excursion

Initial input parameters and equations

Both Sr and Li models were constructed from the basic mass-balance equation with respect to geological time (t), shown here for Sr:

$$\frac{dN_{Sr}}{dt} = F_r + F_h + F_{diag} - F_{sink} \qquad \text{(Eqn. 1)}$$

where N is the total inventory of the seawater Sr reservoir, and F_x represents the input and sink fluxes (r: riverine input; h: hydrothermal input; diag: diagenetic reflux; Note sink for Sr in Eqns. 1 and 2 mainly represents marine carbonate, while for Li in Eqns. 5 and 6, the sink represents combined alteration of oceanic crust and marine authigenic clay formation). The isotopic balance equation is then given by:

$$N_{Sr}\frac{dR_{SW}}{dt} = F_r\,(R_r - R_{SW}) + F_h(R_h - R_{SW}) + F_{diag}(R_{diag} - R_{SW}) - F_{sink}(R_{sink} - R_{SW}) \qquad \text{(Eqn. 2)}$$

where R_x is the isotopic ratio of the different input and sink fluxes. R_{sink} for Sr isotopes is equal to contemporaneous seawater (R_{SW}), as Sr isotopes are not fractionated during marine carbonate precipitation. Calculation of the sink (F_{sink}) from seawater assumes that partitioning into the sink has a constant partition coefficient k, which is determined by Eqn. 3. Residence time is determined by the ratio of reservoir size to oceanic throughput flux, which is determined by Eqn. 4.

$$F_{sink} = k \times N \qquad \text{(Eqn. 3)}$$

$$T_{res} = \frac{N_{Sr}}{F_{sink\ (or\ input)}} = \frac{1}{k} \qquad \text{(Eqn. 4)}$$

The same equation was applied to the Li isotope system, with isotope fractionation between seawater R_{sw} and R_{sink} ($\Delta^7Li_{sink} = R_{sw} - R_{sink}$) being considered, and without adding a diagenetic flux. The flux and isotope balance equations are then given by:

$$\frac{dN_{Li}}{dt} = F_r + F_h - F_{sink} \qquad \text{(Eqn. 5)}$$

$$N_{Li}\frac{dR_{SW}}{dt} = F_r\,(R_r - R_{SW}) + F_h(R_h - R_{SW}) - F_{sink}(R_{sink} - R_{SW}) \qquad \text{(Eqn. 6)}$$

Like the approach applied to Sr isotopes, calculation of the sink (F_{sink}) from seawater assumes that partitioning into the sink has a constant partition coefficient, k (Eqn. 3).

Steady state is assumed prior to running the model, where the input and output flux are balanced. We adjust several initial input parameters from modern values to more closely approximate the Precambrian condition. Referring to Precambrian steady-state mass balance Li cycle (Kalderon-Asael et al., 2021), we doubled the initial hydrothermal flux (F_h) of the modern value for both Sr and Li isotope systems assuming a higher hydrothermal flux (matching higher outgassing/ridge spreading rates (Tajika and Matsui, 1992; Holland, 2009)) than the modern value. Both Li and Sr riverine fluxes (F_r) were calculated to match the measured pre-excursion values. The riverine input $^{87}Sr/^{86}Sr$ ratio was taken from the riverine $^{87}Sr/^{86}Sr$ evolution curve in (Shields, 2007) by binary mixing of the carbonate weathering input and silicate weathering input. The hydrothermal input (R_h) $^{87}Sr/^{86}Sr$ ratio was taken from the mantle evolution curve in (Workman and Hart, 2005). Both R_r (0.7075) and R_h (0.7016) are less radiogenic than the modern value (0.712 and 0.703, respectively), which is more reasonable considering prolonged (~1570 Ma) Rb decay (giving increased $^{87}Sr/^{86}Sr$) for both continental crust and the depleted mantle. Based on a previous study (Richter and Liang, 1993), the Sr isotope ratios of the diagenetic reflux (R_{diag}) from deep-sea sediment was set the same as for contemporary seawater (0.705). Unlike Sr isotopes, lithium isotopes are not influenced by radiogenic decay. The lower R_r for lithium isotopes (5.8‰) relative to the modern (23‰) is based on the modelled riverine input value for the Precambrian (Kalderon-Asael et al., 2021), to fit the general low δ^7Li_{SW} values. The lower riverine input value (Rr) is reasonable, considering the warmer temperature during the studied period, which would lead to less isotope fractionation during clay formation (Li and West, 2014). R_h is normally considered unchanged from the present-day (Coogan and Dosso, 2012). A less effective isotope fractionation (Δ^7Li = 7‰; Kalderon-Asael et al., 2021) than the modern (16‰;

Misra and Froelich, 2012) during Li burial was taken to fit the overall enhanced reverse weathering during the Precambrian, especially during the Mesoproterozoic (Krissansen-Totton and Catling; Kalderon-Asael et al., 2021). The calculated initial residence times for both seawater Sr and Li are close to the modern values (~2 Myr for Sr (Basu et al., 2001); 1.25 Myr for Li (Kalderon-Asael et al., 2021)).

Modelling the positive excursion

Several failed scenarios for explaining the increasing and decreasing trend of the observed Sr and Li isotope excursions are depicted in **Fig. S7 and Fig. S8**, respectively. The increasing trend is explained in detail in the main text. Here, we provide additional discussion on the recovery phase by modeling the subsequent decline (blue band, **Fig. S8**) in seawater Sr and Li isotope values under various scenarios.

A reduction in riverine input flux without altering isotope values leads to a decline in seawater $^{87}Sr/^{86}Sr$. However, because riverine δ^7Li is lower than that of seawater, a reduced weathering flux would result in an increase in seawater δ^7Li—opposite to the observed trend (**Fig. S8a**). Alternatively, decreasing only the riverine isotopic values would require an implausible combination: a ~0.0025 drop in $^{87}Sr/^{86}Sr$ alongside riverine δ^7Li values falling below 0‰, which is lower than the average for primary silicate rocks (Pogge von Strandmann et al., 2021a) (**Fig. S8b**). A final possibility is an increase in hydrothermal input. Our model shows that a ~1.8× increase in hydrothermal flux can account for the observed decline in $^{87}Sr/^{86}Sr$. However, this change alone is not sufficient to reproduce the observed decline in δ^7Li (**Fig. S8c**). This discrepancy can be resolved by invoking a shorter residence time for Li isotopes, consistent with a lower seawater Li inventory during the Precambrian, as discussed in the main text.

While we do not exclude the possibility of combined scenarios, such as a simultaneous decrease in riverine isotope values and increase in hydrothermal flux, enhanced hydrothermal input appears necessary based on current age model constraints. This interpretation is consistent with the tectonic context of the partial breakup of the supercontinent Nuna (Lu et al., 2002), during which increased hydrothermal activity, possibly alongside the weathering of less radiogenic igneous rocks, is highly likely.

Sensitivity tests

We explored the sensitivity of the modelling results to initial input parameters (e.g., hydrothermal input flux, fractionation factors), the duration of the excursion, and uncertainties associated with the age model. In conducting sensitivity tests on the initial input hydrothermal flux (F_h), we varied the values 1.5 times, 2 times and to 3 times the present-day value. The results indicate that increasing the initial hydrothermal input flux would decrease the required continental weathering flux (Fr) from 3.2 times to 2.3 times the initial flux, and would also decrease the required riverine input δ^7Li (Rr) from ~19‰ to ~17‰, to achieve the observed peak of the excursion (**Fig. S9**).

We also investigate the effect of the initial input $\Delta^7Li_{sw\text{-}sink}$ on the modelled results for Li isotopes (**Fig. S10**). We increase and decrease the initial input $\Delta^7Li_{sw\text{-}sink}$ by 50% from the chosen value (7‰), to 10.5‰ and 3.5‰, respectively. We observe changes in the required riverine input δ^7Li from 18‰ to 15‰ and 20.5‰, respectively, to achieve the observed peak in the Li isotope excursion. A lower fractionation factor for $\Delta^7Li_{sw\text{-}sink}$ necessitates a higher riverine input value to achieve the observed seawater δ^7Li peak.

A sensitivity test on the residence time shows that a reduction in the oceanic residence times of Sr and Li would lead to a more rapid recovery and would require a less substantial increase in the weathering flux and riverine δ^7Li to achieve the observed peak values (**Fig. S11a**). Reducing the residence time for both Li and Sr isotopes from twice the modern value to one-third of the modern value requires a decrease in weathering flux from 4 to 1.9 times the initial input, and a reduction in riverine δ^7Li from 21‰ to 14‰. A shortened residence time for Li isotopes is likely, considering increased marine reverse weathering during the Precambrian, which would lower the seawater Li inventory. Reducing the residence time to 1/3 of the modern level allows Li recovery within ~1.2 Myr without external forcing. However, this is not applicable for Sr isotopes, and an external forcing is necessary to achieve lower $^{87}Sr/^{86}Sr$ ratios during the recovery phase relative to the initial values (see main text for further discussion).

The age model and duration of the Sr and Li isotope excursions are constrained by C isotope stratigraphy and based on the assumption of constant sediment accumulation rates. The consequent rate of change in seawater Sr isotopes observed in this study (~0.0007/Myr)

surpasses the maximum rate of change during the Phanerozoic (0.000192/Myr) (McArthur et al., 2012; Zhou et al., 2020). If we recalculate by assuming the most extreme oscillation rate (0.000192/Myr) known for the Phanerozoic ocean, at least ~4 Myr would be required to increase seawater $^{87}Sr/^{86}Sr$ by 0.0007. One potential explanation for this disparity is that the abrupt downward trend in the negative $\delta^{13}C$ excursion is linked to a condensed section (a transgressive package with sea level increase (Loutit et al., 1998). A highly condensed section is associated with the slow accumulation of fine-grained sediments, and therefore represents a more considerable span of time than might otherwise be assumed (Loutit et al., 1988). A sensitivity test on duration (**Fig. S11b**) shows that increasing the duration of the upward trend from 1 to 4 Myrs would result in a decrease in the required weathering flux from 2.7 to 1.8 times, along with a required riverine $\delta^{7}Li$ decrease from 18‰ to 14‰. In this case, our box modelling based on the current age model/duration represents an extreme scenario (i.e., a maximum constraint on the increased weathering flux). A more accurate age model and stratigraphic correlation for the study interval awaits further study, but $^{87}Sr/^{86}Sr$ isotope records hold the potential to contribute to the refinement of future age models.

Except for the uncertainty associated with the duration of the increasing trend, we further test the uncertainties associated with the numerical dating and age model. As mentioned before, U-Pb zircon dating of tuffs provides absolute age constraints at the top and base of Gaoyuzhuang Member III, with 1560 ± 5 Ma (Li et al., 2010) and ~1577 ± 12 Ma (Tian et al., 2015), respectively. In this study, we use the mean value of the numerical dating (i.e., 1560 Ma and 1577 Ma) for age model construction, resulting the excursion duration of ~2 Myrs (~1 Myr increase and ~1 Myr decrease), which is then used in the box modelling. Given the constraints from the Sr isotope record discussed above, our use of a ~2 Myr duration already represents a minimum-case scenario. Therefore, we test the sensitivity of the age model here only for the maximum range based on numerical dating (i.e., 1555 Ma to 1589 Ma). A new age model constructed based on this age range shows a doubled duration for the excursion (~2 Myr increase followed by an ~2 Myr decrease), which requires a 2 times increase in the continental weathering flux (previously 2.8 times), alongside a riverine $\delta^{7}Li$ input of 15‰ (previously 18‰) to reach the peak of the observed Sr and Li isotope excursion (**Fig. S12).**

4. Other factors that might affect the Sr and Li isotope excursions

Sr isotope composition undergoing weathering

A volcanic-induced weathering event is proposed in the main text. Different from extensive basaltic weathering during the Neoproterozoic Era (Cox et al., 2016; Zhou et al., 2020), which drove seawater $^{87}Sr/^{86}Sr$ down due to the weathering of unradiogenic sources, several studies have highlighted that Mesoproterozoic volcanism was characterised by a greater abundance of felsic volcanic activity and granitic formations (Condie et al., 2023; Lu et al., 2023), which are attributed to the recycling of substantial continental crust into the mantle. It has been suggested that the juvenile (low $^{87}Sr/^{86}Sr$) and reworked crust (high $^{87}Sr/^{86}Sr$) in peripheral accretionary orogens were of similar magnitude, yielding a weathered Sr isotope ratio with a relatively consistent value through the Mesoproterozoic Era (Condie, 2021).

In addition, the modelling results suggest that solely increasing or decreasing riverine $^{87}Sr/^{86}Sr$ input ratios are unlikely to explain the observed excursion (**Fig. S8**). Without strong constraints on $^{87}Sr/^{86}Sr$ values, combined changes in Sr isotope ratios of the riverine input and weathering flux could result in unlimited outcomes. For instance, an increase in the $^{87}Sr/^{86}Sr$ riverine input could require a lesser increase in weathering flux to match the observed peak. To simplify, we kept the Sr isotope unchanged to constrain the weathering flux change in our model. Nevertheless, in any scenario, increases in both weathering flux and river δ^7Li values are necessary to achieve the observed Sr and Li isotope excursion. Therefore, the weathering regime change pathway identified in this study remains valid.

Temperature and pH effect on Li isotopes

A temperature effect on the fractionation factor is imposed during Li uptake into clay minerals, which might affect both riverine and seawater δ^7Li without an associated change in weathering rates or regimes (Li and West, 2014). Fractionations during continental weathering and marine reverse weathering give a temperature dependence of −0.25‰/K for seawater Li (Li and West, 2014; Pogge von Strandmann et al., 2021b), whereby higher temperatures will decrease seawater δ^7Li values. Although the low initial riverine input value could partly be a function of temperature, temperature change is obviously not sufficient to drive the observed seawater

excursions (~5‰) on their own and cannot explain the increased seawater δ^7Li trend given the intensive volcanism and warm temperatures of the studied period. Thus, it is unlikely that the observed positive δ^7Li excursion is caused by temperature-induced fractionation effect (Montañez et al., 1996).

The pH effect on the fractionation factor during lithium incorporation into carbonate rocks remains debated. While some studies have reported a negative covariation between pH and δ^7Li in foraminifera (Roberts et al., 2018), others have found no such effect (Vigier et al., 2015; Charrieau et al., 2023). Research on inorganic carbonates has detected either no pH-related effects (Day et al., 2021; Branson Oscar, 2024) or minimal effects within a reasonable pH range (Füger et al., 2019, 2022). Thus, the observed ~5% increase in inorganic carbonate δ^7Li in this study is less likely to be solely driven by changes in seawater pH. Additionally, in fluids such as seawater, the fractionation values may differ from experimental findings due to variations in the bonding environment of lithium in the solid (Füger et al., 2022). Given the current information, a detailed discussion and definite conclusion on the pH effect is problematic and lies beyond the scope of this study.

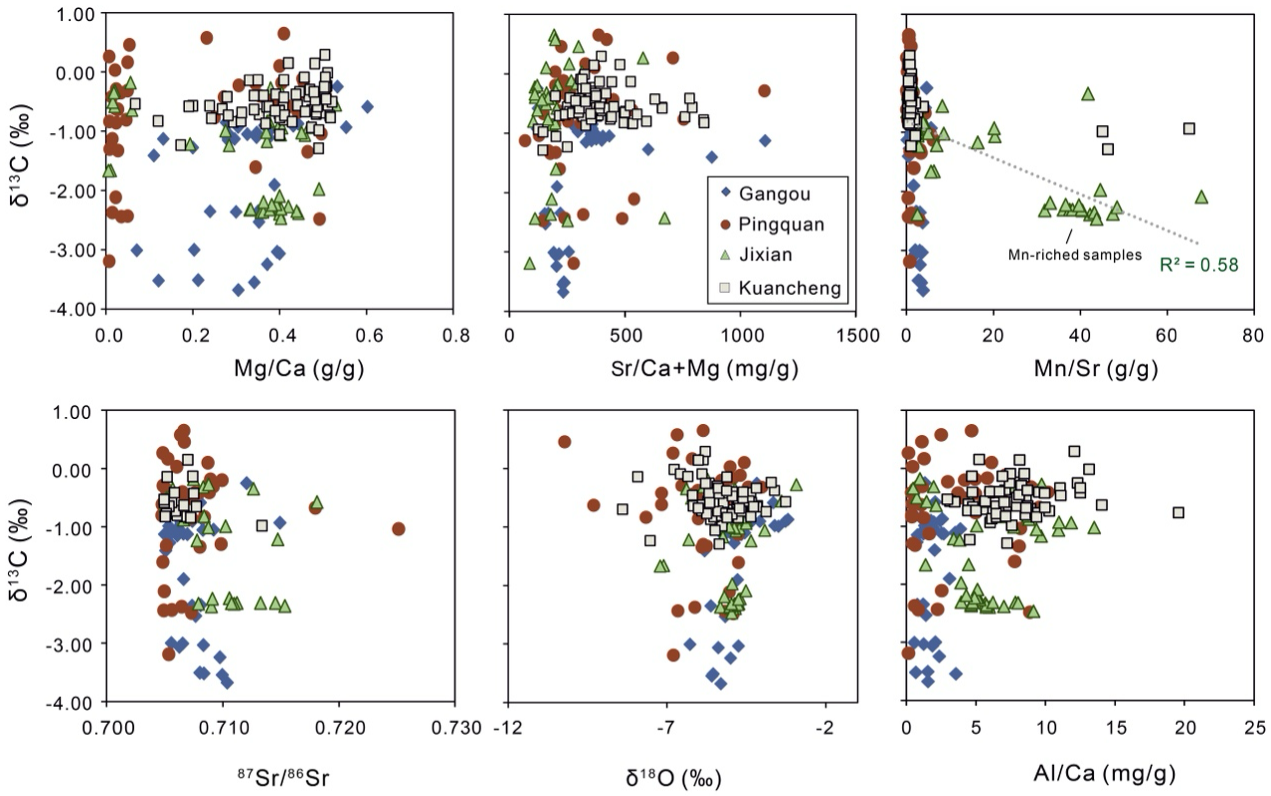

Figure S1. Cross plot of measured $\delta^{13}C_{carb}$ with diagenetic and clay contamination indices. Errors are smaller than the symbols used.

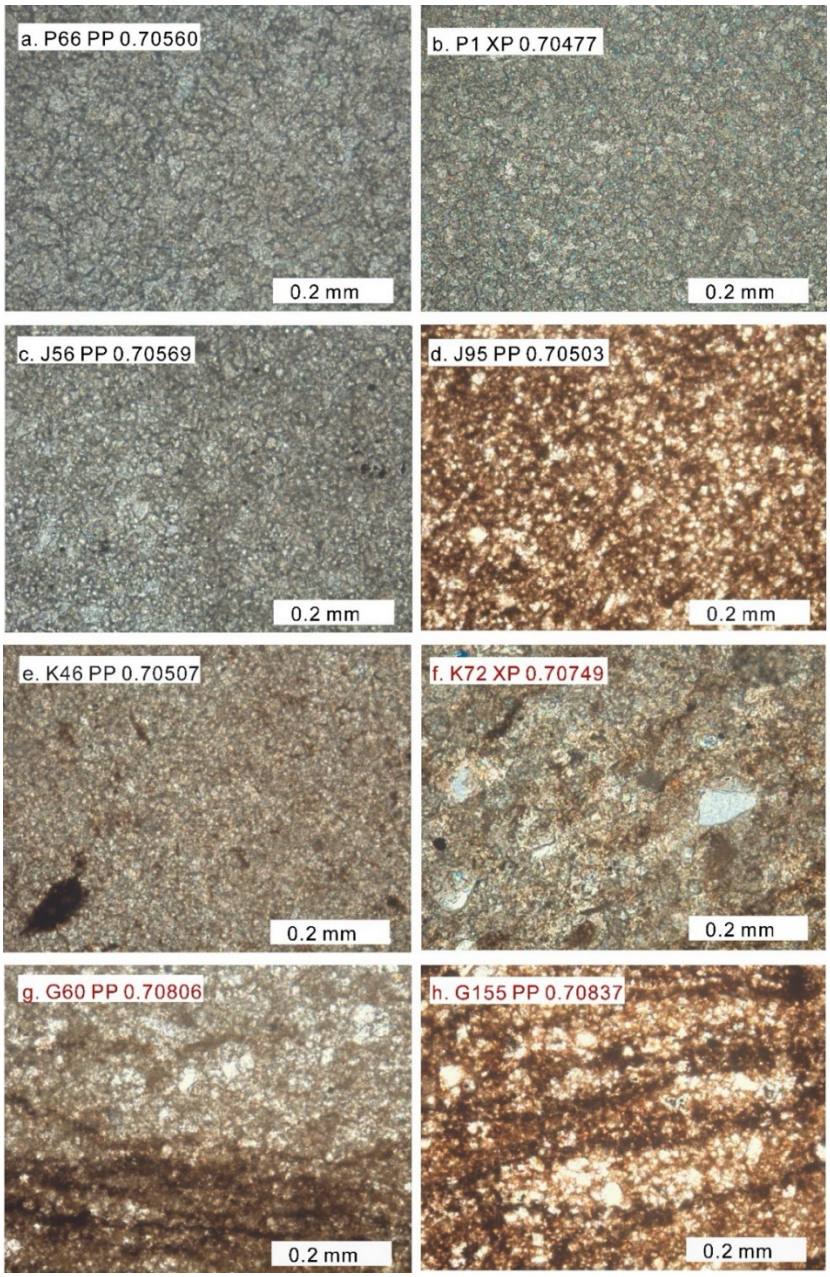

Figure S2. Microscopic features of the Gaoyuzhuang Formation in the studied area. The top left label is shown as: sample name followed by plane-polarized light (PP) or cross-polarized light (XP), followed by Sr isotope ratio. For instance, "P66 PP 0.70560" means sample P66 (Pingquan section) is shown in plane-polarized light, with a Sr isotope ratio of 0.70560. The scale of all images is 0.2 mm. P66 (a) and J56 (c) are limestone samples that mark the peak in Sr and Li isotopes.

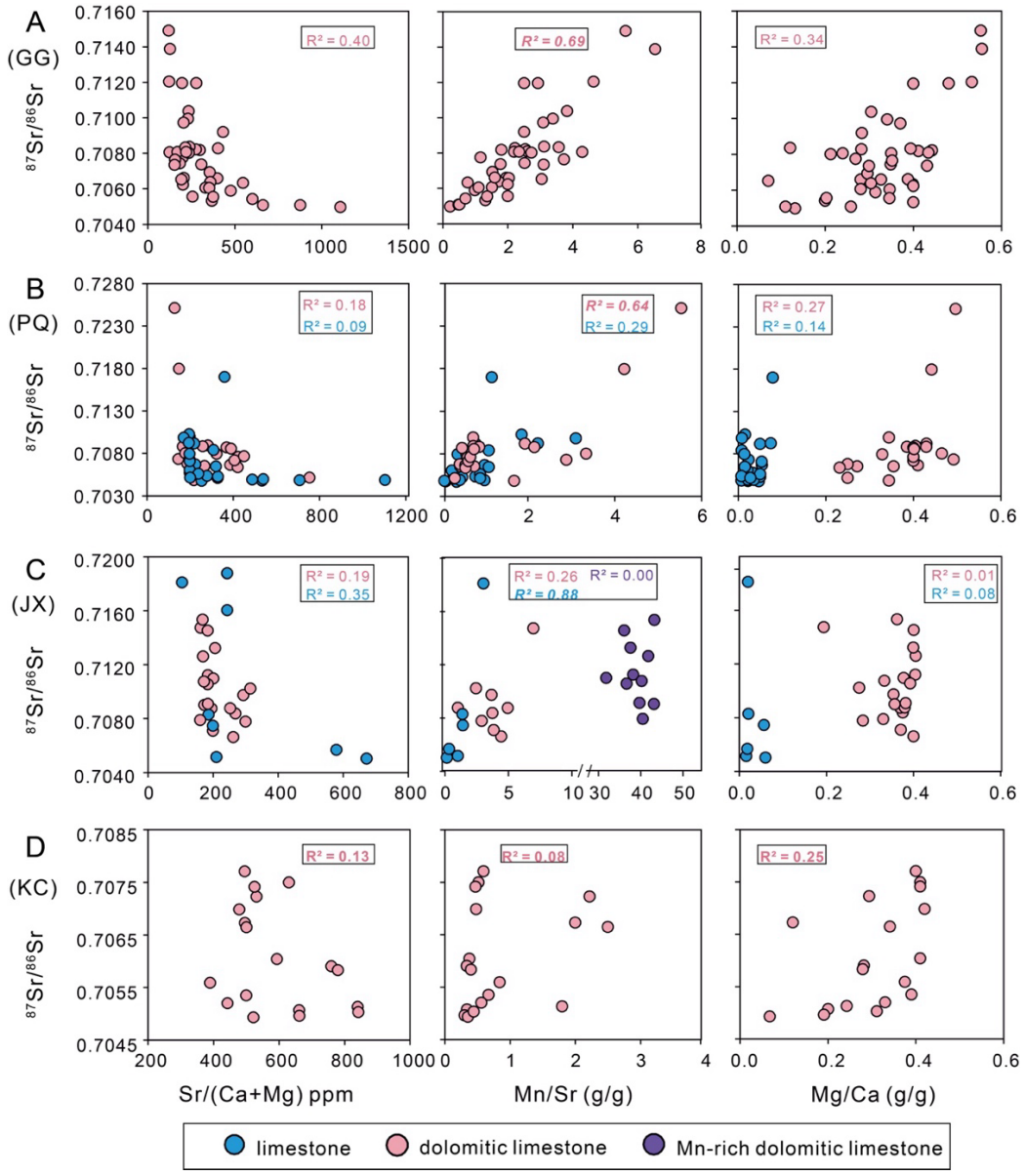

Figure S3. Step 1: Diagenetic screening. Cross plot of $^{87}Sr/^{86}Sr$ versus bulk carbonate Sr/Ca+Mg, Mn/Sr, and Mg/Ca (in 2% HNO3) for each section. A) GG: Gangou section; B) PQ: Pingquan section; C) JX: Jixian section; D) KC: Kuancheng section. $R^2 > 0.5$ shown in bold italics. Errors are smaller than the symbols used.

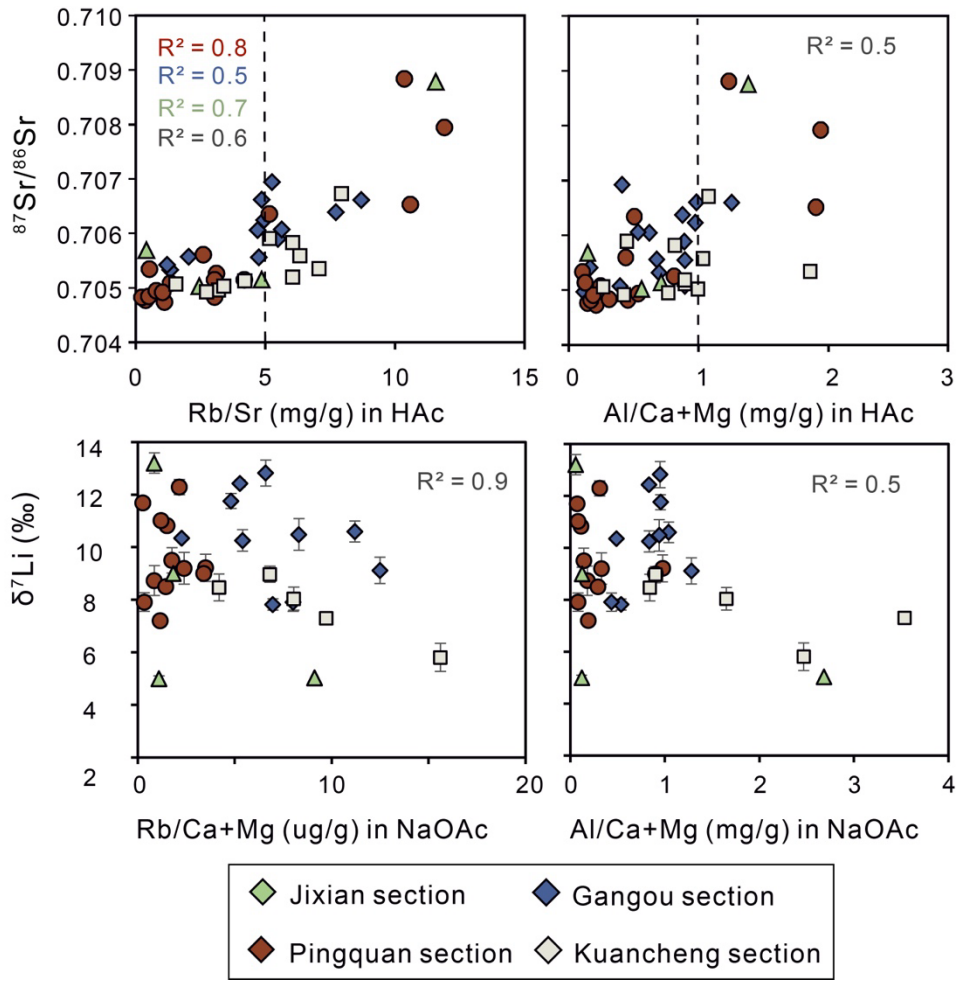

Figure S4. Step 2: Clay contamination screening. For samples passing screening step 1, cross plots are shown for $^{87}Sr/^{86}Sr$ versus Rb/Sr and Al/(Ca+Mg) in the Sr leachate (HAc), and δ^7Li versus Rb/Ca+Mg and Al/Ca+Mg in the Li leachate (NaOAc). Only correlations with $R^2 > 0.5$ are shown (colours represent the corresponding section shown in the legend). Error bars for δ^7Li represent 2 SD (N =3) of the replicates for each sample.

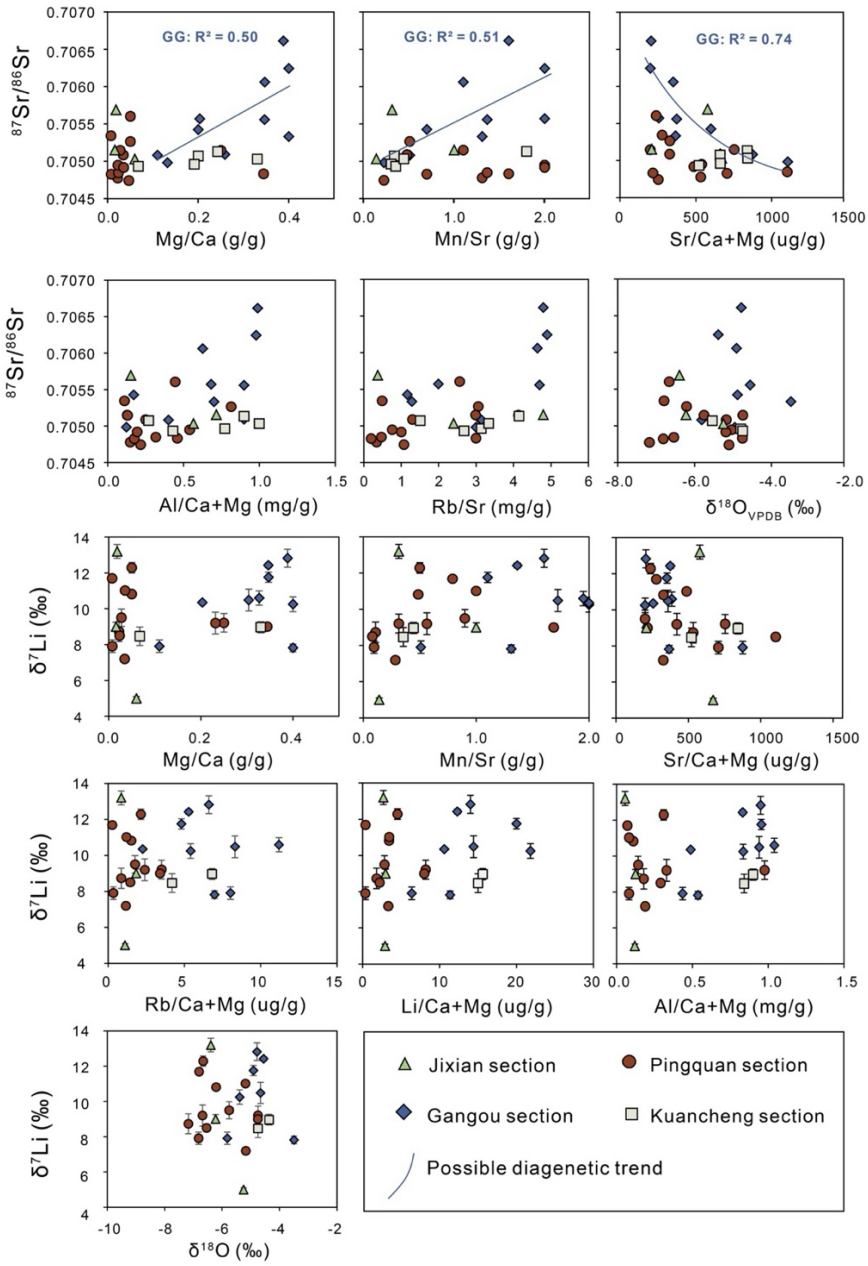

Figure S5. Step 3: Cut off validity evaluation: $^{87}Sr/^{86}Sr$ and δ^7Li values of samples that passed cut offs in steps 1-2 versus indicators of diagenesis and detrital contamination. Only trendlines with $R^2 \geq 0.5$ are shown. Apart from $^{87}Sr/^{86}Sr$ ratios in the Gangou (GG) section, $^{87}Sr/^{86}Sr$ ratios in the other three sections and δ^7Li for all sections show no signs of alteration. All Mg/Ca, Mn/Sr and Sr/(Ca+Mg) ratios are from bulk carbonate (in 2% HNO_3). For Sr isotope plots, Rb/Sr and Al/(Ca+Mg) are from Sr isotope leachates (in HAc); For Li isotope plots, Al/(Ca+Mg), Rb/(Ca+Mg) and Li/(Ca+Mg) are from Li isotope leachates (in NaOAc). Error bars for δ^7Li represent 2 SD (N = 3) of the replicates for each sample.

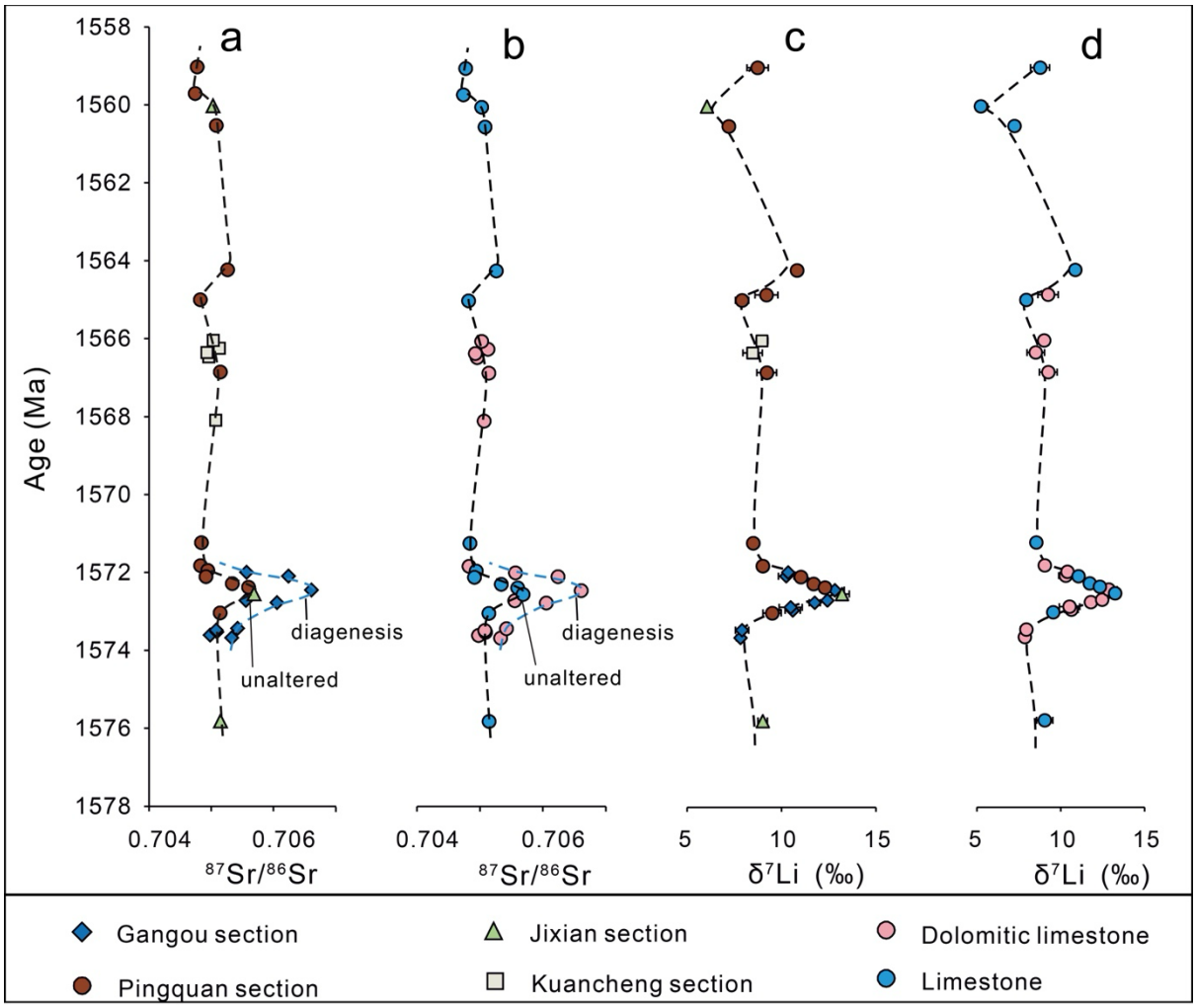

Figure S6. Step 4: Section comparison. Sr and Li isotopes for samples that passed cut offs in the first two steps are distinguished by stratigraphic level (a, c) and Mg/Ca ratios (b. d). Black dashed line shows trend for unaltered samples (δ^7Li refers to measured values), blue dashed line shows diagenetically altered samples with higher $^{87}Sr/^{86}Sr$ ratios from the Gangou section dolomitic limestone (consistent with the diagenetic trend in Fig. S6). Error bars for δ^7Li represent 2 SD (N = 3) of the replicates for each sample.

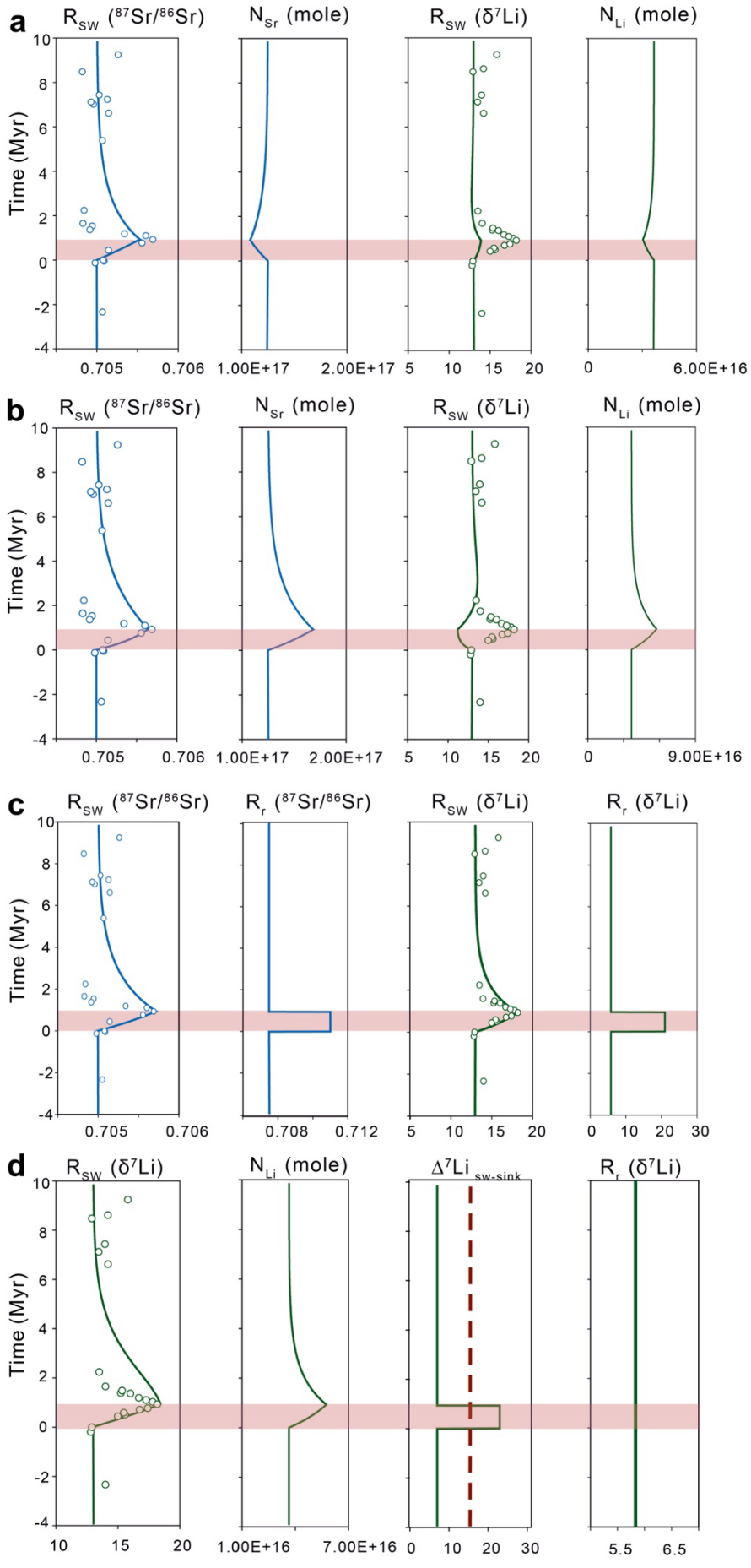
a
R_{SW} ($^{87}Sr/^{86}Sr$)
N_{Sr} (mole)
R_{SW} (δ^7Li)
N_{Li} (mole)
Time (Myr)
10
8
6
4
2
0
-2
-4
0.705
0.706
1.00E+17
2.00E+17
5
10
15
20
0
6.00E+16
b
R_{SW} ($^{87}Sr/^{86}Sr$)
N_{Sr} (mole)
R_{SW} (δ^7Li)
N_{Li} (mole)
Time (Myr)
0.705
0.706
1.00E+17
2.00E+17
5
10
15
20
0
9.00E+16
c
R_{SW} ($^{87}Sr/^{86}Sr$)
R_r ($^{87}Sr/^{86}Sr$)
R_{SW} (δ^7Li)
R_r (δ^7Li)
Time (Myr)
0.705
0.706
0.708
0.712
5
10
15
20
0
10
20
30
d
R_{SW} (δ^7Li)
N_{Li} (mole)
$\Delta^7Li_{sw\text{-}sink}$
R_r (δ^7Li)
Time (Myr)
10
15
20
1.00E+16
7.00E+16
0
10
20
30
5.5
6.5

Figure S7. Modelling the increasing trend (red band) for seawater Sr and Li isotopes for different scenarios. N: total inventory of the seawater elemental reservoir, R_{sw}: seawater isotope values, R_r: riverine input isotope values, $\Delta^7Li_{sw\text{-}sink}$: fractionation between seawater and sink (combined alteration of the oceanic crust and marine authigenic clay formation). A) Decreasing only the hydrothermal flux: a 10x decrease in F_h is required to achieve the seawater Sr isotope peak, but this does not produce the seawater Li isotope peak. B) Increasing only the riverine input flux: seawater δ^7Li and $^{87}Sr/^{86}Sr$ proceed in different directions. C) Increasing only riverine input isotope values (R_r): an increase of 0.0035 for riverine $^{87}Sr/^{86}Sr$ and 15‰ for riverine δ^7Li is required to achieve both peaks. Such an increase in riverine Sr isotope input in 1 Myr is unrealistic. D) Given the riverine input flux constrained by Sr isotopes, an increase in $\Delta^7Li_{sw\text{-}sink}$ alone requires an increase from 7‰ to 23‰ (higher than the modern value; shown as red dashed line) to achieve the seawater δ^7Li peak, which is unrealistic for the Mesoproterozoic. Errors for δ^7Li are smaller than the symbols used.

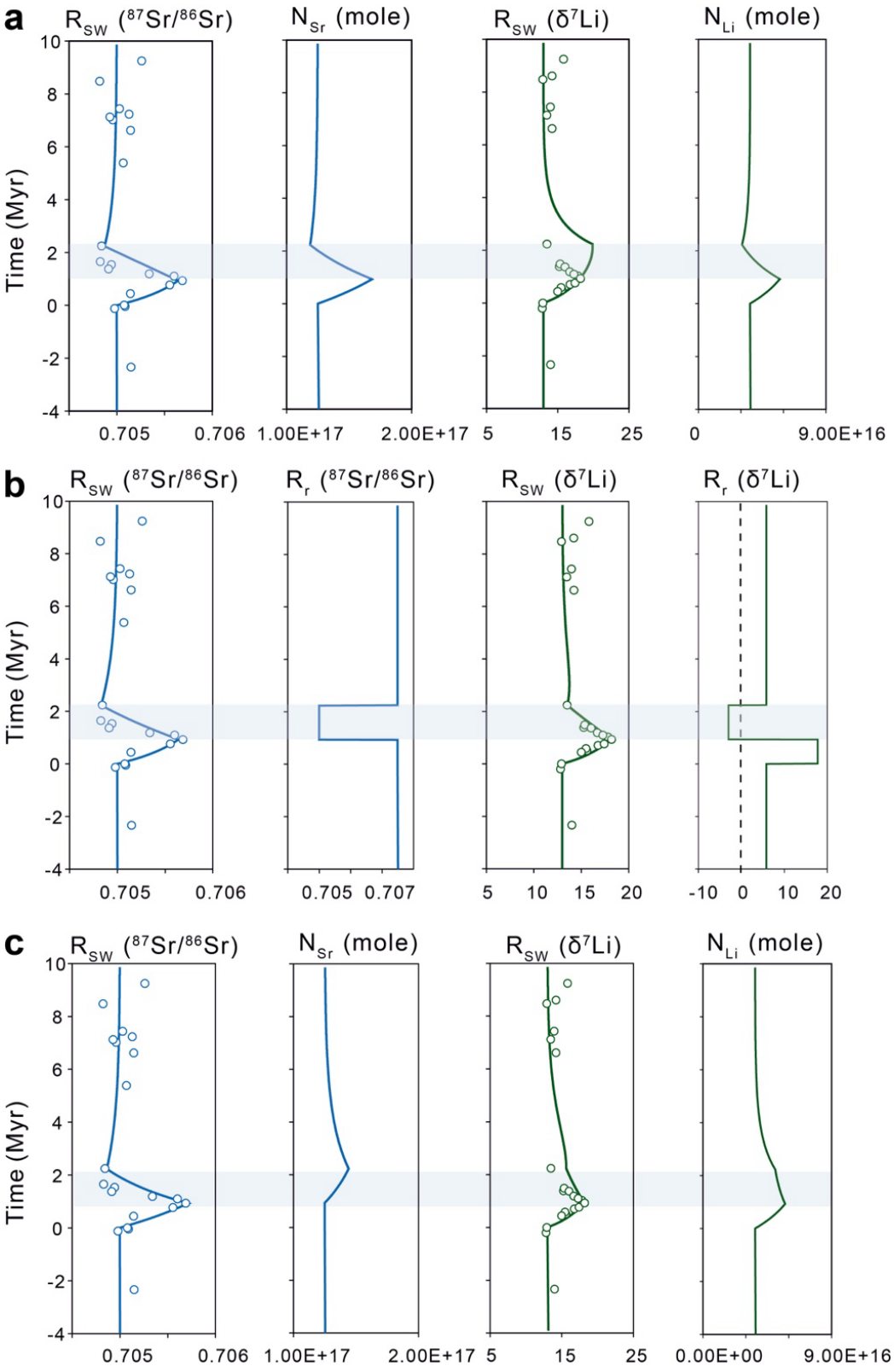
a
R_{SW} ($^{87}Sr/^{86}Sr$)
N_{Sr} (mole)
R_{SW} (δ^7Li)
N_{Li} (mole)
Time (Myr)
10
8
6
4
2
0
-2
-4
0.705
0.706
1.00E+17
2.00E+17
5
15
25
0
9.00E+16
b
R_{SW} ($^{87}Sr/^{86}Sr$)
R_r ($^{87}Sr/^{86}Sr$)
R_{SW} (δ^7Li)
R_r (δ^7Li)
Time (Myr)
0.705
0.706
0.705
0.707
5
10
15
20
-10
0
10
20
c
R_{SW} ($^{87}Sr/^{86}Sr$)
N_{Sr} (mole)
R_{SW} (δ^7Li)
N_{Li} (mole)
Time (Myr)
0.705
0.706
1.00E+17
2.00E+17
5
15
25
0.00E+00
9.00E+16

Figure S8. Modelling the decreasing trend (blue band) for sea water Sr and Li isotopes for different scenarios. A) Decreasing only the riverine input flux: seawater δ^7Li increases rather than decreases. B). Decreasing only the riverine input isotope values (R_r): a decrease of 0.0025 for riverine $^{87}Sr/^{86}Sr$ and a value lower than 0‰ for riverine δ^7Li is required to achieve both nadirs, which is unrealistic. C) Increasing only the hydrothermal flux: a 1.8 times increase in F_h is required to achieve the measured Sr isotope ratio, but this is not sufficient for δ^7Li. Errors for δ^7Li are smaller than the symbols used.

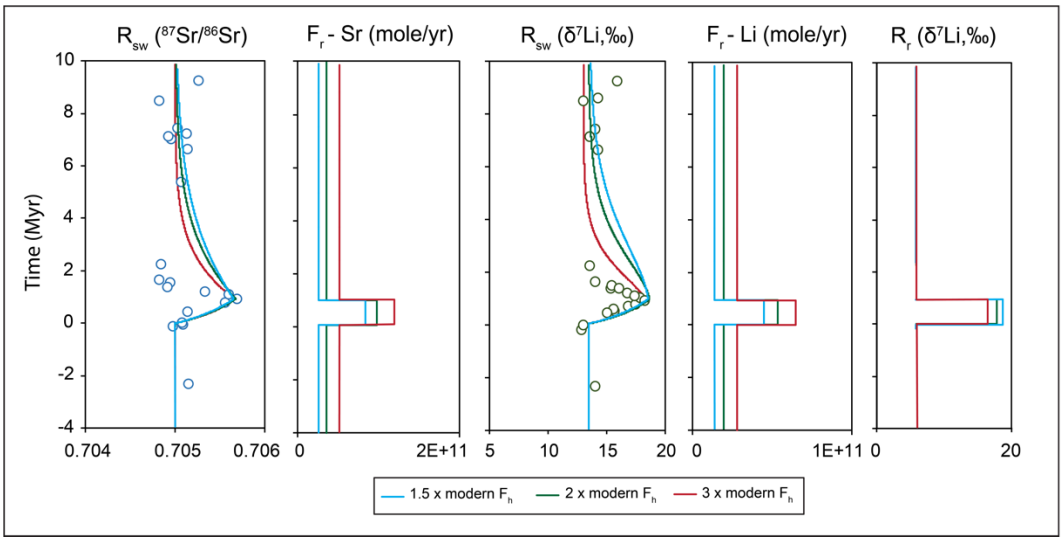

Figure S9. Sensitivity test for the initial input hydrothermal flux. Initial inputs of 1.5, 2 and 3 times the modern hydrothermal flux requires a 3.2, 2.7 and 2.3 times increase in the continental weathering flux (Fr), along with a 13‰, 12‰ and 11‰ increase in river δ^7Li, respectively, to achieve the observed Sr and Li isotope excursions. Without external forcing for recovery, a higher initial hydrothermal input flux results in a shorter residence time and a faster recovery rate. Errors are smaller than the symbols used.

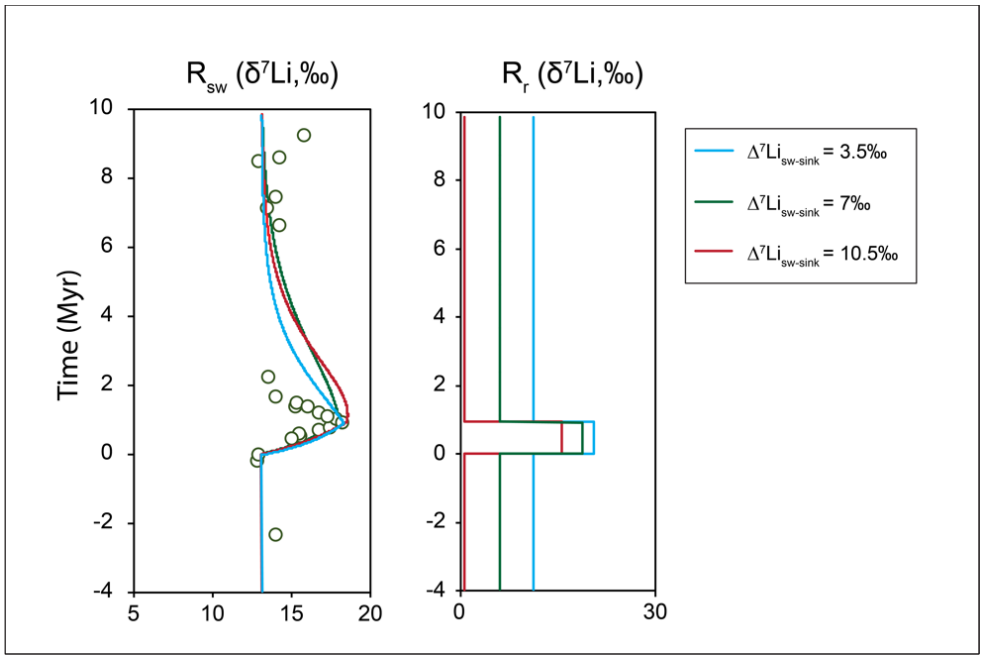

Figure S10. Sensitivity test for initial input $\Delta^7Li_{sw\text{-}sink}$. Initial riverine input δ^7Li (Rr) values are adjusted accordingly for initial mass balance. For the initial $\Delta^7Li_{sw\text{-}sink}$ of 3.5‰, 7‰ and 10.5‰, the required changes for Rr are from 11.3‰ to 20.5‰, from 5.8‰ to 18‰, and from 0.4‰ to 15‰, respectively, to achieve the observed peak in the Li isotope excursion. Errors for δ^7Li are smaller than the symbols used.

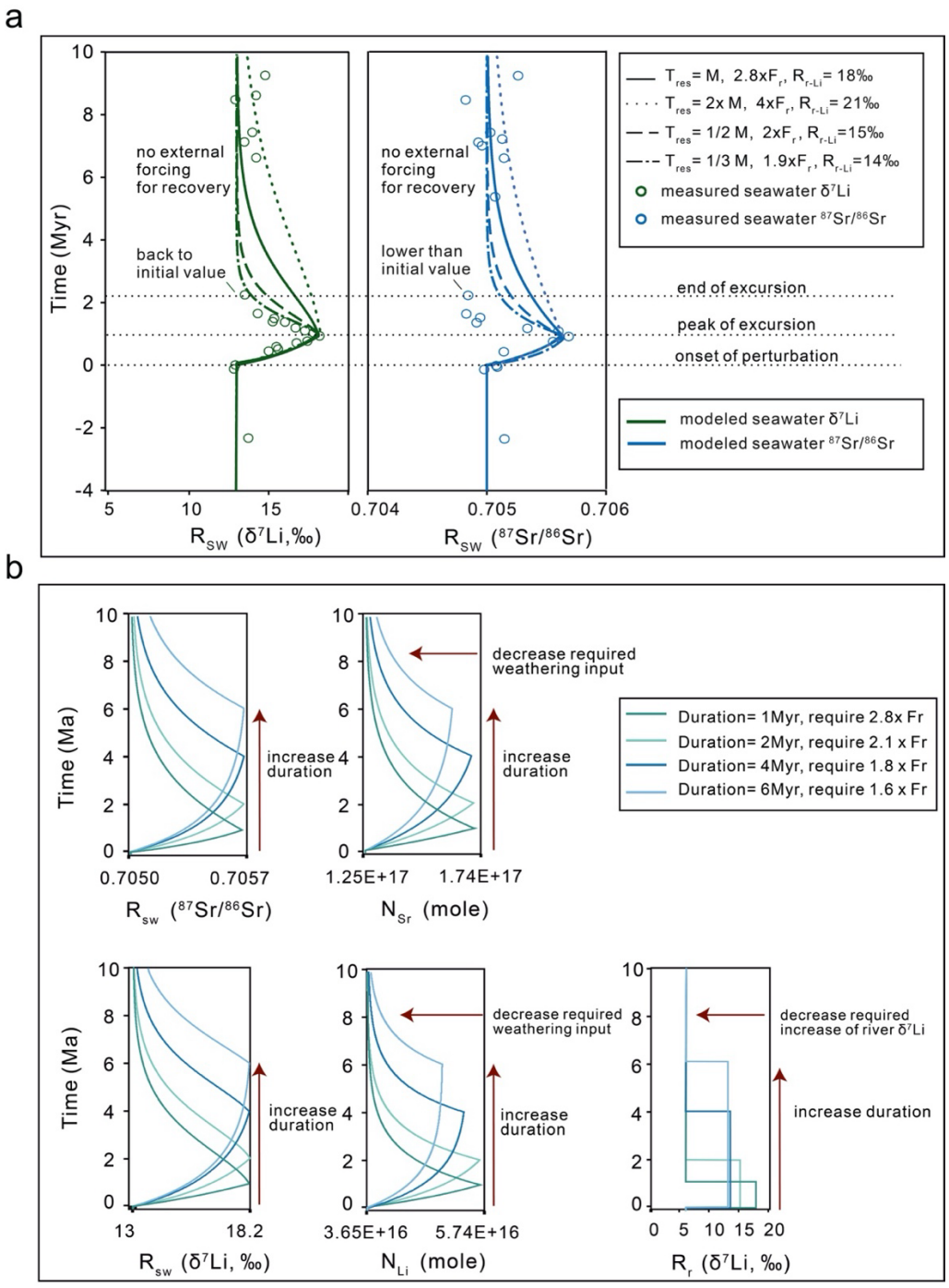

Figure S11. Sensitivity test for a) different residence time, and b) different duration for increasing trend. a) Reducing residence time would require less of an increase in F_r and riverine δ^7Li ($R_{r\text{-}Li}$) to achieve the peak value, and would lead to a rapid recovery without external forcing. b) Longer duration for increasing trend would require less of an increase in F_r and riverine δ^7Li (R_r).

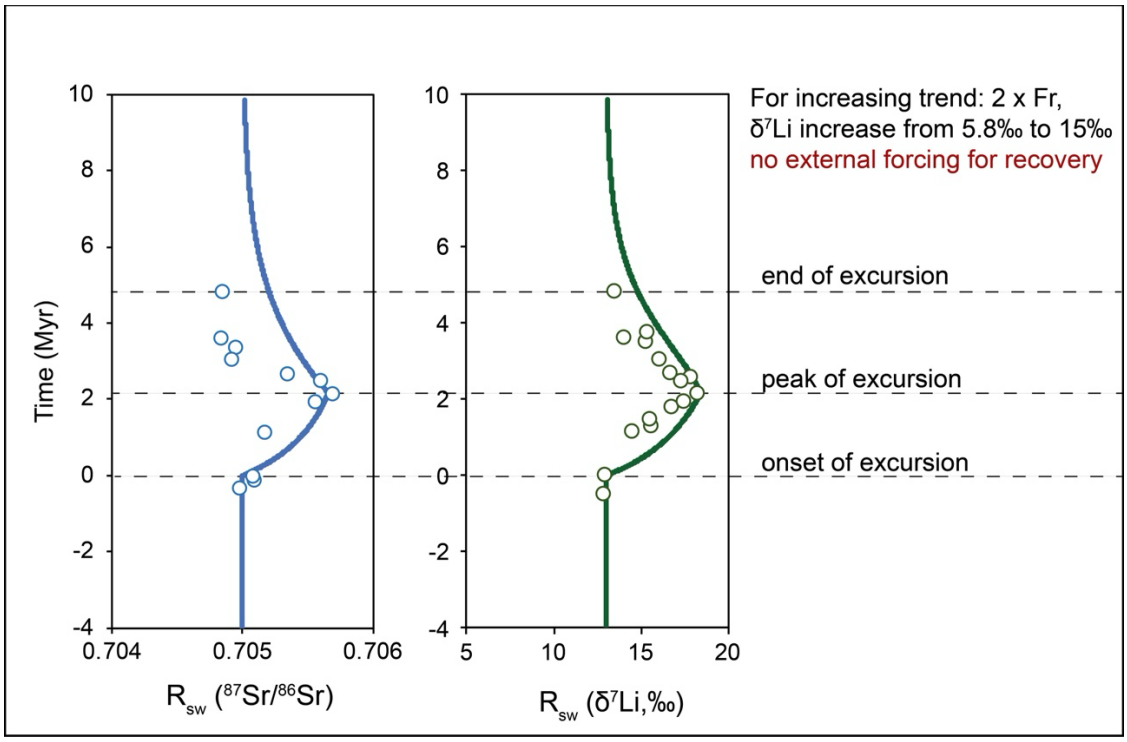

Figure S12. Sensitivity test for age model. A sensitivity test is conducted for the maximum age range based on the numerical dating (e.g., from 1555 Ma to 1589 Ma). A new age model constructed based on this age range shows a longer duration (~2 Myr increase followed by a ~2 Myr decrease) compared to the previous age model (Fig. 3 in main text), which requires a lower increase in the continental weathering flux (2 times) and a lower riverine δ^7Li input (15‰) to reach the peak of the observed Sr and Li isotope excursion. Errors are smaller than the symbols used.

Table S1. Initial model input parameters and references.

	Sr	Notes/Reference for Sr	Li	Notes/Reference for Li
F_r (mol/yr)	3.46×10^{10}	calculated from this study for initial mass balance	1.88×10^{10}	calculated from this study for initial mass balance
F_h (mol/yr)	2.54×10^{10}	(Nana Yobo et al., 2021), double the modern value	1.04×10^{10}	(Kalderon-Asael et al., 2021), double the modern value
F_{diag} (mol/yr)	5.50×10^{9}	(Peucker-Ehrenbrink and Fiske, 2019), same as modern value		
F_{sink} (mol/yr)	6.55×10^{10}	equal to total input flux ($F_r + F_h + F_{diag}$)	2.92×10^{10}	equal to total input flux ($F_r + F_h$)
R_r	0.7075	(Shields, 2007)	5.8 ‰	(Kalderon-Asael et al., 2021)
R_h	0.7016	(Shields, 2007)	6.3 ‰	(Coogan and Dosso, 2012)
$\Delta^7Li_{sw\text{-}sink}$			7 ‰	(Kalderon-Asael et al., 2021)
R_{diag}	0.7050	equal to measured R_{sw}		
R_{sink}	0.7050	equal to measured R_{sw}	6 ‰	$R_{sw} - \Delta^7Li_{sw\text{-}sink}$
N_{sw} (mole)	1.25×10^{17}	(Palmer and Edmond, 1989), same as modern	3.65×10^{16}	(Pogge Von Strandmann et al., 2013), same as modern
R_{sw}	0.7050	measured from this study	13 ‰	measured from this study
T_{res}	2×10^6	calculated, similar as modern (Basu et al., 2001)	1.25×10^6	calculated, similar as modern (Kalderon-Asael et al., 2021)

References

Basu, A.R., Jacobsen, S.B., Poreda, R.J., Dowling, C.B., and Aggarwal, P.K., 2001, Large groundwater strontium flux to the oceans from the bengal basin and the marine strontium isotope record: Science, v. 293, doi:10.1126/science.1060524.

Branson Oscar, U.J.B.S.M.M.S., 2024, Controls on Li partitioning and isotopic fractionation in inorganic calcite: Geochimica et Cosmochimica Acta, v. 382, p. 91–102.

Charrieau, L.M., Rollion-Bard, C., Terbrueggen, A., Wilson, D.J., Pogge von Strandmann, P.A.E., Misra, S., and Bijma, J., 2023, Controls on Lithium Incorporation and Isotopic Fractionation in Large Benthic Foraminifera: Minerals, v. 13, doi:10.3390/min13010127.

Chen, X., and Zhou, Y., 2023, Effective Leaching of Argillaceous and Dolomitic Carbonate Rocks for Strontium Isotope Stratigraphy: Geostandards and Geoanalytical Research, doi:10.1111/ggr.12531.

Chen, X., Zhou, Y., and Shields, G.A., 2022, Progress towards an improved Precambrian seawater 87Sr/86Sr curve: Earth-Science Reviews, v. 224, doi:10.1016/j.earscirev.2021.103869.

Condie, K.C., 2021, Revisiting the Mesoproterozoic: Gondwana Research, v. 100, p. 44–52, doi:10.1016/j.gr.2020.08.001.

Condie, K.C., Pisarevsky, S.A., Puetz, S.J., Roberts, N.M.W., and Spencer, C.J., 2023, A-type granites in space and time: Relationship to the supercontinent cycle and mantle events: Earth and Planetary Science Letters, v. 610, doi:10.1016/j.epsl.2023.118125.

Coogan, L.A., and Dosso, S., 2012, An internally consistent, probabilistic, determination of ridge-axis hydrothermal fluxes from basalt-hosted systems: Earth and Planetary Science Letters, v. 323–324, doi:10.1016/j.epsl.2012.01.017.

Cox, G.M., Halverson, G.P., Stevenson, R.K., Vokaty, M., Poirier, A., Kunzmann, M., Li, Z.X., Denyszyn, S.W., Strauss, J. V., and Macdonald, F.A., 2016, Continental flood basalt weathering as a trigger for Neoproterozoic Snowball Earth: Earth and Planetary Science Letters, v. 446, p. 89–99, doi:10.1016/j.epsl.2016.04.016.

Crockford, P.W. et al., 2021, Reconstructing Neoproterozoic seawater chemistry from early diagenetic dolomite: Geology, v. 49, doi:10.1130/G48213.1.

Day, C.C., Pogge von Strandmann, P.A.E., and Mason, A.J., 2021, Lithium isotopes and partition coefficients in inorganic carbonates: Proxy calibration for weathering reconstruction: Geochimica et Cosmochimica Acta, v. 305, doi:10.1016/j.gca.2021.02.037.

Dellinger, M. et al., 2018, The Li isotope composition of marine biogenic carbonates: Patterns and mechanisms: Geochimica et Cosmochimica Acta, v. 236, doi:10.1016/j.gca.2018.03.014.

Dellinger, M., Hardisty, D.S., Planavsky, N.J., Gill, B.C., Kalderon-Asael, B., Asael, D., Croissant, T., Swart, P.K., and West, A.J., 2020, The effects of diagenesis on lithium isotope ratios of shallow marine carbonates: American Journal of Science, v. 320, doi:10.2475/02.2020.03.

Fang, H., Tang, D., Shi, X., Lechte, M., Shang, M., Zhou, X., and Yu, W. Manganese-rich deposits in the Mesoproterozoic Gaoyuzhuang Formation (ca. 1.58 Ga), North China platform: Genesis and paleoenvironmental implications: Palaeogeography, Palaeoclimatology, Palaeoecology, doi:10.1016/j.palaeo.2020.109966.

Füger, A., Konrad, F., Leis, A., Dietzel, M., and Mavromatis, V., 2019, Effect of growth rate and pH on lithium incorporation in calcite: Geochimica et Cosmochimica Acta, v. 248, doi:10.1016/j.gca.2018.12.040.

Füger, A., Kuessner, M., Rollion-Bard, C., Leis, A., Magna, T., Dietzel, M., and Mavromatis, V., 2022, Effect of growth rate and pH on Li isotope fractionation during its incorporation in calcite: Geochimica et Cosmochimica Acta, v. 323, doi:10.1016/j.gca.2022.02.014.

Gorokhov, I.M., Kuznetsov, A.B., Vasil'eva, I.M., Konstantinova, G. V., Dubinina, E.O., Lipenkov, G. V., and Rizvanova, N.G., 2022, Sr and Pb Isotopic Compositions in Dolostones of the Lower Riphean Billyakh Group, Anabar Uplift: Step-Leaching Technique in Chemostratigraphy and Geochronology: Stratigraphy and Geological Correlation, v. 30, doi:10.1134/S0869593822040049.

Guo, H., Du, Y., Kah, L.C., Huang, J., Hu, C., Huang, H., and Yu, W., 2013, Isotopic composition of organic and inorganic carbon from the Mesoproterozoic Jixian Group, North China: Implications for biological and oceanic evolution: Precambrian Research, doi:10.1016/j.precamres.2012.09.023.

Higgins, J.A., Bla, C.L., Lundstrom, E.A., Santiago-ramos, D.P., Akhtar, A.A., Cru, A., Bialik, O., Holmden, C., and Bradbury, H., 2018, ScienceDirect Mineralogy , early marine diagenesis , and the chemistry of shallow-water carbonate sediments: v. 220, p. 512–534, doi:10.1016/j.gca.2017.09.046.

Holland, H.D., 2009, Why the atmosphere became oxygenated: A proposal: Geochimica et Cosmochimica Acta, v. 73, doi:10.1016/j.gca.2009.05.070.

Kalderon-Asael, B. et al., 2021, A lithium-isotope perspective on the evolution of carbon and silicon cycles: Nature, v. 595, doi:10.1038/s41586-021-03612-1.

Krissansen-Totton, J., and Catling, D.C. A coupled carbon-silicon cycle model over Earth history: Reverse weathering as a possible explanation of a warm mid-Proterozoic climate: Earth and Planetary Science Letters, doi:10.1016/j.epsl.2020.116181.

Li, G., and West, A.J., 2014, Evolution of Cenozoic seawater lithium isotopes: Coupling of global denudation regime and shifting seawater sinks: Earth and Planetary Science Letters, v. 401, doi:10.1016/j.epsl.2014.06.011.

Li, H., Zhu, S., Xiang, Z., Su, W., Lu, S., Zhou, H., Geng, J., Li, S., and Yang, F., 2010, Zircon U-Pb dating on tuff bed from Gaoyuzhuang Formation in Yanqing, Beijing: Further constraints on the new subdivision of the Mesoproterozoic stratigraphy in the northern North China Craton: Acta Petrologica Sinica, v. 26, p. 2131–2140.

Liu, X.F., Liu, X.M., Wang, X.K., Zhai, S., and Liu, X., 2023, Dolostone as a reliable tracer of seawater lithium isotope composition: Communications Earth and Environment, v. 4, doi:10.1038/s43247-023-00711-x.

Liu, G., Zhang, S., Li, H., Bao, X., Zhao, H., Liang, D., Wu, H., Tang, D., Zhu, X., and Yang, T., 2022, Cyclostratigraphic calibration of the ca. 1.56 Ga carbon isotope excursion and oxygenation event recorded

in the Gaoyuzhuang Formation, north China: Global and Planetary Change, v. 216, doi:10.1016/j.gloplacha.2022.103916.

Loutit, T.S., Hardenbol, J., Vail, P.R., and Baum, G.R., 1988, Condensed sections: the key to age determination and correlation of continental margin sequences: Sea-level changes: an integrated approach, doi:10.2110/pec.88.01.0183.

Lu, G.M., Wang, W., Ernst, R.E., El Bilali, H., Spencer, C.J., Xu, Y.G., and Bekker, A., 2023, Evolutionary stasis during the Mesoproterozoic Columbia-Rodinia supercontinent transition: Precambrian Research, v. 391, doi:10.1016/j.precamres.2023.107057.

Lu, S., Yang, C., Li, H., and Li, H., 2002, A Group of Rifting Events in the Terminal Paleoproterozoic in the North China Craton: Gondwana Research, doi:10.1016/s1342-937x(05)70896-0.

Marriott, C.S., Henderson, G.M., Belshaw, N.S., and Tudhope, A.W., 2004, Temperature dependence of δ7Li, δ44Ca and Li/Ca during growth of calcium carbonate: Earth and Planetary Science Letters, v. 222, doi:10.1016/j.epsl.2004.02.031.

McArthur, J.M., Howarth, R.J., and Shields, G.A., 2012, Strontium Isotope Stratigraphy: The Geologic Time Scale 2012, v. 1–2, p. 127–144, doi:10.1016/B978-0-444-59425-9.00007-X.

Misra, S., and Froelich, P.N., 2012, Lithium isotope history of cenozoic seawater: Changes in silicate weathering and reverse weathering: Science, v. 335, p. 818–823, doi:10.1126/science.1214697.

Montañez, I.P., Banner, J.L., Osleger, D.A., Borg, L.E., and Bosserman, P.J., 1996, Integrated Sr isotope variations and sea-level history of middle to Upper Cambrian platform carbonates: Implications for the evolution of Cambrian seawater 87Sr/86Sr: Geology, doi:10.1130/0091-7613(1996)024<0917:ISIVAS>2.3.CO;2.

Murphy, J.G., Ahm, A.S.C., Swart, P.K., and Higgins, J.A., 2022, Reconstructing the lithium isotopic composition (δ7Li) of seawater from shallow marine carbonate sediments: Geochimica et Cosmochimica Acta, v. 337, doi:10.1016/j.gca.2022.09.019.

Nana Yobo, L., Brandon, A.D., Holmden, C., Lau, K. V., and Eldrett, J., 2021, Changing inputs of continental and submarine weathering sources of Sr to the oceans during OAE 2: Geochimica et Cosmochimica Acta, v. 303, doi:10.1016/j.gca.2021.03.013.

Palmer, M.R., and Edmond, J.M., 1989, The strontium isotope budget of the modern ocean: Earth and Planetary Science Letters, v. 92, p. 11–26, doi:10.1016/0012-821X(89)90017-4.

Peucker-Ehrenbrink, B., and Fiske, G.J., 2019, A continental perspective of the seawater 87Sr/86 Sr record: A review: Chemical Geology, v. 510, p. 140–165, doi:10.1016/j.chemgeo.2019.01.017.

Pogge von Strandmann, P.A.E., Dellinger, M., and West, A.J., 2021a, Lithium Isotopes: A Tracer of Past and Present Silicate Weathering: Elements in Geochemical Tracers in Earth System Science,.

Pogge von Strandmann, P.A.E., Frings, P.J., and Murphy, M.J., 2017, Lithium isotope behaviour during weathering in the Ganges Alluvial Plain: Geochimica et Cosmochimica Acta, v. 198, p. 17–31, doi:10.1016/j.gca.2016.11.017.

Pogge von Strandmann, P.A.E., Jenkyns, H.C., and Woodfine, R.G., 2013, Lithium isotope evidence for enhanced weathering during Oceanic Anoxic Event 2: Nature Geoscience, v. 6, doi:10.1038/ngeo1875.

Pogge von Strandmann, P.A.E., Jones, M.T., Joshua West, A., Murphy, M.J., Stokke, E.W., Tarbuck, G., Wilson, D.J., Pearce, C.R., and Schmidt, D.N., 2021b, Lithium isotope evidence for enhanced weathering and erosion during the Paleocene-Eocene Thermal Maximum: Science Advances, v. 7, doi:10.1126/sciadv.abh4224.

Pogge von Strandmann, P.A.E., Schmidt, D.N., Planavsky, N.J., Wei, G., Todd, C.L., and Baumann, K.H., 2019, Assessing bulk carbonates as archives for seawater Li isotope ratios: Chemical Geology, v. 530, p. 119338, doi:10.1016/j.chemgeo.2019.119338.

Richter, F.M., and Liang, Y., 1993, The rate and consequences of Sr diagenesis in deep-sea carbonates: Earth and Planetary Science Letters, v. 117, doi:10.1016/0012-821X(93)90102-F.

Roberts, J., Kaczmarek, K., Langer, G., Skinner, L.C., Bijma, J., Bradbury, H., Turchyn, A. V., Lamy, F., and Misra, S., 2018, Lithium isotopic composition of benthic foraminifera: A new proxy for paleo-pH reconstruction: Geochimica et Cosmochimica Acta, v. 236, doi:10.1016/j.gca.2018.02.038.

Shang, M., Tang, D., Shi, X., Zhou, L., Zhou, X., Song, H., and Jiang, G., 2019, A pulse of oxygen increase in the early Mesoproterozoic ocean at ca. 1.57–1.56 Ga: Earth and Planetary Science Letters, v. 527, p. 115797, doi:10.1016/j.epsl.2019.115797.

Shields, G., 2007, A normalised seawater strontium isotope curve: possible implications for Neoproterozoic-Cambrian weathering rates and the further oxygenation of the Earth: eEarth, v. 2, p. 35–42, doi:10.5194/ee-2-35-2007.

Tajika, E., and Matsui, T., 1992, Evolution of terrestrial proto-CO2 atmosphere coupled with thermal history of the earth: Earth and Planetary Science Letters, v. 113, doi:10.1016/0012-821X(92)90223-I.

Tian, H. et al., 2015, Zircon LA-MC-ICPMS U-Pb dating of tuff from Mesoproterozoic Gaoyuzhuang Formation in Jixian County of North China and its geological significance: Acta Geoscientica Sinica, v. 36, p. 647–658.

Vahrenkamp, V.C., and Swart, P.K., 1990, New distribution coefficient for the incorporation of strontium into dolomite and its implications for the formation of ancient dolomites: Geology, v. 18, doi:10.1130/0091-7613(1990)018<0387:NDCFTI>2.3.CO;2.

Vigier, N., Rollion-Bard, C., Levenson, Y., and Erez, J., 2015, Lithium isotopes in foraminifera shells as a novel proxy for the ocean dissolved inorganic carbon (DIC): Comptes Rendus - Geoscience, v. 347, doi:10.1016/j.crte.2014.12.001.

Workman, R.K., and Hart, S.R., 2005, Major and trace element composition of the depleted MORB mantle (DMM): Earth and Planetary Science Letters, doi:10.1016/j.epsl.2004.12.005.

Zhang, K., Zhu, X., Wood, R.A., Shi, Y., Gao, Z., and Poulton, S.W., 2018, Oxygenation of the Mesoproterozoic ocean and the evolution of complex eukaryotes: Nature Geoscience, v. 11, p. 345–350, doi:10.1038/s41561-018-0111-y.

Zhou, Y., von Strandmann, P.A.E.P., Zhu, M., Ling, H., Manning, C., Li, D., He, T., and Shields, G.A., 2020, Reconstructing tonian seawater 87Sr/86Sr using calcite microspar: Geology, v. 48, p. 462–467, doi:10.1130/G46756.1.